

NEXT-GENERATION INTEGRATED PHOTONICS:
GRAPHENE AND OPTICAL PHASED ARRAYS

A Dissertation

Presented to the Faculty of the Graduate School

of Cornell University

in Partial Fulfillment of the Requirements for the Degree of

Doctor of Philosophy

by

Christopher Thomas Phare

December 2017

© 2017 Christopher Thomas Phare

ALL RIGHTS RESERVED

NEXT-GENERATION INTEGRATED PHOTONICS: GRAPHENE AND
OPTICAL PHASED ARRAYS

Christopher Thomas Phare, Ph.D.

Cornell University 2017

Silicon photonics, the design and manufacturing of optical structures on silicon wafers using the same process as computer chips, has in the past several years revolutionized high-speed communications between computers and stands primed to further advance sensing, signal processing, and quantum computation. Such photonic devices are the most powerful because they can be manufactured at incredible scale, allowing us to either build them very cheaply or build large systems of photonic components, much like transistors and large-scale integrated circuits. In this dissertation we make a leapfrog improvement in the state of the art of silicon photonics in two different areas: dramatically improving the performance of modulators using graphene and building large-scale silicon optical phased arrays with record-breaking efficiency and output beam quality.

The dissertation is divided into five chapters. In the first, I introduce silicon photonics, discuss its capabilities and limitations, and summarize the key results of the dissertation. In Chapter 2, I lay a theoretical framework for on-chip waveguides and ring resonators with a mathematical notation used throughout the thesis, as well as derive Fourier optics of optical phased arrays from first-principle scattering theory. Chapter 3 details work on graphene ring modulators, including extensive fabrication and measurement details. Chapter 4 continues with theoretical and experimental models of using graphene for highly linear and purely phase-based

modulators. Finally, Chapter 5 describes work on chip-scale optical phased arrays and a method for achieving half-wavelength emitter waveguide pitch.

BIOGRAPHICAL SKETCH

Christopher Thomas Phare was born in February 1990 in Columbus, Ohio. He moved in 2002 to Birmingham, Alabama, where he attended the Jefferson County International Baccalaureate School and got his first serious exposure to scientific research by devoting excessive amounts of time to science fair projects. He graduated from Vanderbilt University in 2011 with a Bachelor of Arts degree in physics and mathematics with highest honors. While there, he worked on several projects, from ultrafast laser spectroscopy under Professor Norman Tolk, to computational and mathematical models of photonic crystal biosensors under Professor Sharon Weiss. Additionally, he spent a summer at Cornell University under the Cornell NanoScale Science and Technology Facility's Research Experience for Undergraduates program, where he worked with Professor Jiwoong Park on hybrid graphene-pentacene thin-film transistors. Chris returned to the Hill after graduating, joining Professor Michal Lipson's nanophotonics group. He received the Masters of Science degree in 2015 before moving with the group to Columbia University to finish his doctoral studies.

Gradatim ferociter.

ACKNOWLEDGEMENTS

The stereotype of the solo academic could not be further from the truth. The PhD is inherently social and collaborative, alternately tiring and energizing, and both frustrating and marvelous. I am forever indebted to the people who have made it so. I have tried to name as many as possible in a few paragraphs here; the inevitable omissions have been no less important.

First, I must thank my thesis advisor Professor Michal Lipson. Over the past six years she has been an unparalleled mentor and group leader who has enabled all of the research here. Michal convinces us that the impossible is indeed possible and holds the group to a work ethic and productivity that ensures our research will continually be at the forefront. Her tireless work ensures the group is never lacking equipment, resources, or willing collaborators. Whenever an idea is expensive, speculative, or unfunded we are encouraged to stop worrying and just get things done.

Beyond simple mastery at research management, Michal exudes kindness and relentless optimism. When we all inevitably fail at one research problem or another fab process, Michal picks us up, places us back on our feet, and sets us off again with renewed belief in the future of our research. This attitude spills over (certainly deliberately) to the rest of the group. She has created a group culture where students can work freely without fear of internal competition and where we are all genuine friends.

I would also like to thank the rest of my special committee, Professors Alexander Gaeta and Clifford Pollock. They have rounded out my studies with both a pure physics and application-centric focus, and have always been available to discuss research problems and career goals. Even their Q-exam quizzes on wave equations and amplifier design are fond memories.

Perhaps the biggest contribution to this dissertation and my overall PhD life has been the fellow members of my research group, in no particular order: Aseema Mohanty and Avik Dutt, with whom I started together and shared every year of the PhD; Steven Miller and Romy Fain, who joined only one year later and graduated with us; Yoon Ho Daniel Lee, Lawrence Tzuang, Bishu Guha, Mian Zhang, Lian Luo, Kevin Luke, Austin Griffith, and Mohammad Soltani, who taught me everything about how to do photonics research; Jaime Cardenas and Carl Poitras, the research associates who have been infinite sources of technical advice; and Samantha Roberts, Mohammad Amin Tadayon, Brian Lee, Ipshita Datta, Xingchen William Ji, Tong Lin, Min Chul Shin, Brian Stern, Oscar Jimenez Gordillo, Gaurang Bhatt, Moshe Zadka, Euijae Shim, Utsav Dave, and You-Chia Chang, who have taught me as much as I have them and to whom I entrust the future of the lab. All of these people have been not just coworkers and research collaborators, but my closest friends, who make coming to the office each day worthwhile. I will miss them dearly in the years ahead.

I have also had the great fortune to meet many fellow graduate students outside of my own group, who have made the best set of collaborators and friends. I would particularly like to mention Jared Strait, Pari Nene, Haining Wang, Melina Blee, Changjian Julia Zhang, Nathan Abrams, Jahnvi Sharma, and Sohail Ahasan, each of whom have had their own special contribution to this thesis. The Cornell University Chorus and Glee Club likewise lifted me through good and bad days alike while working on project after project, and the roughly seventy friends and musical co-conspirators I met there make up the largest, most welcoming family I have ever had.

Staff at the Cornell NanoScale Science and Technology Facility, especially John Treichler, Garry Bordonaro, Noah Clay, Phil Infante, and Rob Ilic, as well as Kit

Umbach at the Cornell Center for Materials Research, have helped solve many fabrication-related problems to enable the ideas detailed here. A well-staffed clean-room is essential to pushing the boundaries of nanophotonics, and the CNF has been an unparalleled place to spend a large fraction of my waking life at Cornell. Similarly, industry collaborators, like Kyle Watson and Jinendra Ranka at Trex Enterprises, Oleg Mukhanov, Igor Vernik, and Daniel Yohannes at Hypres, Inc., and David Hutchison, Woosung Kim, and Haisheng Rong at Intel, have enriched my experience beyond the purely academic.

A number of funding sources have made this research possible, from a National Science Foundation Graduate Research Fellowship (DGE-1144153) that enabled me to pursue graphene unfettered in my first years in the group, to a series of other grants from the NSF (ECCS-0335765, DMR-1120296, EEC-0812072), ONR (N00014-16-1-2219), NASA (NNX16AD16G), Hypres (CU15-3985, CU15-3759), and DARPA (HR0011-16-C-0107, HR0011100720034, FA8650-16-7643).

I would also like to thank a decades-long mentor, Dr. Margaret Morrison, who has nurtured my curiosity and guided my intellectual development from an early age. She insists I was professor-like even back when we met while I was in third grade, and I am happy to have at least somewhat fulfilled that prophesy by completing a PhD.

Finally, I must wholeheartedly thank my dear parents. They have been infinitely supportive of my education, fighting essentially since I was born for the absolute best. Thank you for taking my fourth-grade self to high school biology classes, driving halfway across the city each day of middle and high school so I could be continually challenged, and watching me travel across the country and be home far less than I should, simply so I could have the brightest possible future. I will never be able to repay you, but I hope to always make you proud.

TABLE OF CONTENTS

Biographical Sketch	iii
Dedication	iv
Acknowledgements	v
Table of Contents	viii
1 Introduction	1
2 Technical Background	5
2.1 Waveguides	5
2.2 Directional Couplers	9
2.3 Ring Resonators	11
2.4 Fourier Optics for Optical Phased Arrays	16
3 Graphene Ring Modulator	22
3.1 Device Concept	22
3.2 Design and Fabrication	25
3.2.1 Graphene Transfer	27
3.2.2 Surface Planarization	28
3.2.3 Deep-UV Lithography and Patterning	31
3.2.4 Metal-Graphene Contacts	32
3.3 Measurements and Analysis	34
3.3.1 DC Measurements	34
3.3.2 Small-signal RF Measurements	36
3.3.3 Large-signal RF Measurements and Eye Diagrams	36
3.3.4 Conclusion	38
4 Graphene Linear and Phase Modulation	40
4.1 Linear Modulation	40
4.1.1 Device Concept	40
4.1.2 Modulator Fabrication	42
4.1.3 Linearity Measurement and Spurious-free Dynamic Range	44
4.1.4 Theoretical Model	46
4.2 Binary Phase Modulation	48
5 Half-wavelength Pitch Optical Phased Array	54
5.1 Device Concept	54
5.2 Beam Steering Experiment	56
5.2.1 Device Design and Fabrication	56
5.2.2 Far-field Measurement	57
5.2.3 Analysis and Discussion	59
5.3 Phased array beam convergence algorithm	62
Bibliography	66

CHAPTER 1

INTRODUCTION

Silicon photonics, over the past two decades, has transformed from a preposterous idea to an unbelievable success story [1,2]. Devices that use silicon not as a semiconductor for electronics but as a light-guiding material for optics are now routine, with dedicated processes available in commercial foundries [3] and products in volume production for datacenter networking [4]. Most applications today center around high-speed fiber-optic data transmission, and core to these innovations is the silicon modulator [5,6], a fast optical amplitude controller that converts GHz-speed electrical voltage signals into changes in transmission of a laser beam. As we look to the future, however, silicon photonics clearly must grow in two directions: increasingly higher-performance electro-optic devices like modulators, and leveraging the power of integration into large systems afforded by wafer-scale fabrication.

Despite its successes, silicon remains fundamentally limiting as we push to faster modulators and diverse systems. Fast silicon devices depend on single-crystal silicon on insulator (SOI) wafers, which are both expensive, at odds with the requirements of co-fabricated CMOS transistors, and transparent only to a limited range of infrared wavelengths. Additionally, silicon's relatively low mobility itself limits the speed of modulators that use it as the electrically-active material. For nonlinear, quantum, and visible photonics especially we prefer lower-loss and broadly-transparent materials like silicon nitride [7–10], but because silicon nitride is an insulator (bandgap of approximately 5 eV), for active devices generally we have no choice but to use elemental silicon.

Graphene has attracted great interest in electronics for its unparalleled carrier mobility and novel physics [11, 12], yet the performance of graphene photonic devices to date has been limited. While several groups have explored photodetectors made from this single-atom-thick sheet of carbon [13–18], successful demonstrations of modulators have been disappointing, universally having speeds at or below 1 GHz and high unwanted insertion losses.

Here we propose and fabricate a graphene electro-optic modulator based on a novel ring resonator design that operates over an order of magnitude faster than any graphene modulator previously demonstrated. We are also the first to demonstrate high-speed large-signal modulation, showing the capabilities of graphene modulators for serial data transmission. Additionally, the modulator is the first to make use of passive silicon nitride waveguides rather than silicon, opening the door to integrating ultrafast electro-optic components on any passive waveguide material.

A reliable fabrication process for waveguide-based graphene devices then opens a wide array of possible devices. We explore two: a linearized low-distortion modulator for analog signals, and a device design that converts purely absorptive modulation in the graphene to phase modulation of the optical beam.

Linear modulators are especially important for carrying radiofrequency signals over fiber links [19], for routing signals to remote cell towers or satellite links with far less loss than in electrical cables. We realize that graphene, because of its unique linear band structure and capacitive drive, is particularly well-suited for linear modulation. This stands in contrast to inherently nonlinear diode-based modulators common in silicon photonics. Graphene’s impressive linearity (20-30

dB more linear than even specially designed silicon modulators) combined with promise of record-breaking speeds opens up millimeter-wave over fiber links.

Phase modulation, particularly binary (BPSK) or quadrature (QPSK) modulation where phase is modulated in discrete steps, increases the effective data rate of a modulator even further, since these modulation formats have both higher signal-to-noise ratio and can encode a greater number of bits per clock period. Using the phase characteristics of a ring resonator, we unexpectedly find that we can achieve pure binary phase modulation simply by adjusting the round-trip loss of the ring.

Having addressed the design of individual components, we then turn to the frontier of large systems. Wafer-scale structures become their most powerful when integrated in large numbers, yet few researchers today demonstrate more than a handful of photonic components functioning together on one chip. We push these limits by building an optical phased array—a chip-scale device that forms and steers a free-space beam using no moving parts. These arrays consist of large numbers (between tens and thousands) of waveguides, each with its own electrically-controlled phase shifter. When the phases are properly aligned, light emitting from these waveguides constructively interferes in the direction of interest. Modifying the phase across the emitting waveguides then allows us to tilt and focus the beam arbitrarily.

Optical phased arrays today can steer only over a small range of angles (typically $< \pm 25^\circ$) because of limitations on how closely packed waveguides can be on-chip without incurring crosstalk that disrupts the beam. By introducing an anti-crosstalk design, we break this limitation, showing beam formation over $\pm 60^\circ$ in a 64-element array. Our method is the only known way to achieve wide-angle beam steering while keeping almost all of the light focused in the desired beam.

Our continued work to scale up such phased arrays will enable high-performance LIDAR (laser radar) for self-driving cars and precision robotics.

CHAPTER 2

TECHNICAL BACKGROUND

2.1 Waveguides

Waveguides act as the ubiquitous building block in all of integrated photonics. At the most basic, a waveguide consists of a high-index core surrounded by a low-index cladding. In our case, the core is generally silicon (Si, $n = 3.48$ at 1550 nm wavelength [20]) or silicon nitride (Si_3N_4 , $n \approx 2$), while the cladding is silicon dioxide (SiO_2 , $n = 1.44$ [21]), though the options are vast, limited only by transparency at the wavelength of interest. We start with a blanket layer of the high-index material on a thick layer of the low-index one, and then pattern the high-index material via lithography and etching [22]. Optionally, we deposit a cladding layer of a low-index material over the entire structure. Air-clad waveguides without this deposited layer are useful for devices like sensors where the optical mode needs to be exposed, but clad devices are far more robust since they are protected from dust and moisture in the air. The end result of this fabrication process is a rectangular wire of high-index material which confines light laterally and vertically as the light propagates down the wire's length. The structure is very similar to optical fiber, which uses a doped-glass core and an undoped glass cladding instead of etched semiconductor materials.

We build a simple model of light propagation in these waveguides by noting that Maxwell's equations are linear (at least at low intensities) and thus we can formulate electromagnetism as an eigenvalue problem [23]. For waveguides that have translational symmetry in the propagation (z) axis:

$$\mathbf{E}(x, y, z, t) = \mathbf{E}_0(x, y)e^{-i\omega t}e^{i\beta z} \quad (2.1)$$

where at a wave angular frequency ω we separate out an eigenvector \mathbf{E}_0 , the spatial mode profile, and its eigenvalue β , the wavenumber or propagation constant. Throughout we use the convenient trick of representing fields as their complex amplitudes, knowing that the actual fields are the real part of these expressions. The wavenumber β (sometimes written k , and related to the effective index n_{eff}) governs the longitudinal pattern in the waveguide and sets the wavelength inside the material, exactly like the refractive index for a plane wave through a homogeneous dielectric.

$$\beta = k = \frac{2\pi}{\lambda} = n_{\text{eff}}k_0 = n_{\text{eff}}\frac{2\pi}{\lambda_0} \quad (2.2)$$

For waveguides, then, solving the cross-sectional refractive index profile for \mathbf{E}_0 and n_{eff} at the wavelength of interest is the key problem. For some simple cases of high symmetry and low index contrast between core and cladding, closed-form solutions to the mode problem are well-studied [24,25]. For high-index waveguides of interest here, however, analytical methods are inaccurate and we depend on computational solutions to the mode problem. Finite-element and finite-difference electromagnetic solvers are widely available, such as the COMSOL, Photon Design FIMMWAVE [26], and Lumerical MODE software packages. A few example mode profiles of silicon and silicon nitride waveguides are shown in Figure 2.1.

Varying the width and height of the waveguide gives us tremendous control over its optical properties. We can increase the width or height of the waveguide to confine light more strongly inside the waveguide core material, or decrease them to force the optical energy into the surrounding material. Carrying optical energy in

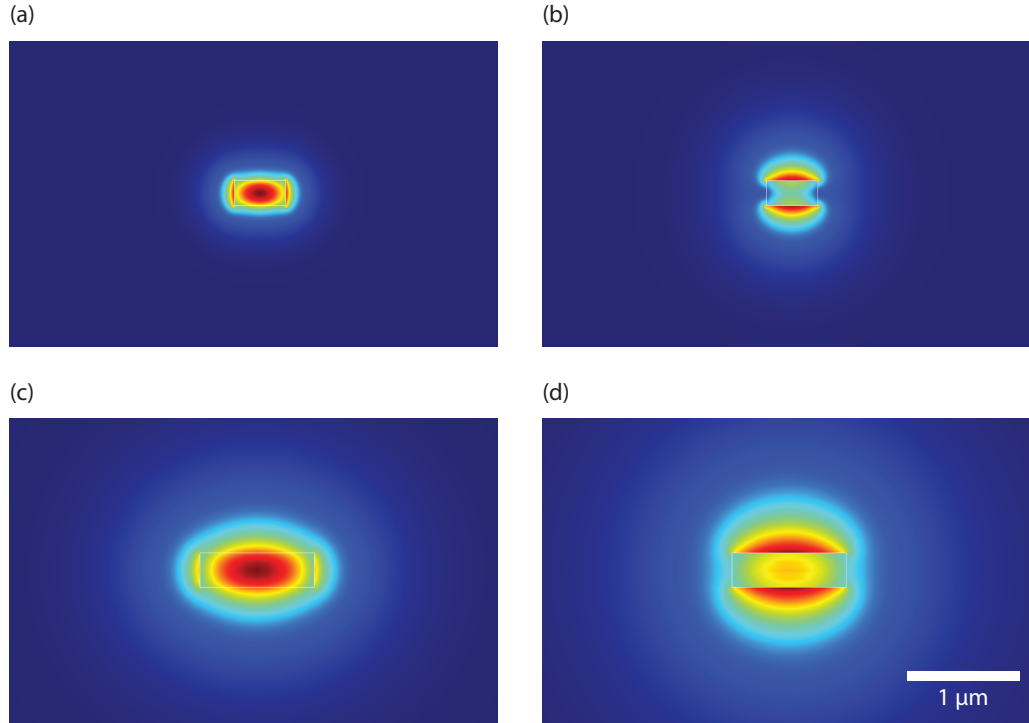


Figure 2.1: Cross-section plots of $|E|$ for several modes. **a.** 450 nm wide by 220 nm tall silicon, TE_0 . **b.** Si, TM_0 . **c.** 1000 nm wide by 300 nm tall silicon nitride, TE_0 . **d.** SiN, TM_0 . All plots are at the same scale.

the cladding is useful when the optically-active material of interest (e.g. graphene, Chapter 3) is not the waveguide core. Changing overlaps between the core and cladding also modifies the effective index of the mode (Figure 2.2), which governs its propagation speed and coupling behavior with adjacent waveguides (Chapter 5), as well as its dispersion, useful for nonlinear optics.

Absent other constraints, we generally choose the waveguide width that minimizes propagation loss, the amount of light lost from the waveguide per unit length. In most waveguides, losses are dominated not by material absorption but by scattering from the rough sidewalls of the waveguide. Roughness is introduced mostly during lithography, from a combination of image blur and random chemical processes in the resist for deep-UV optical lithography [27,28] or from random shot

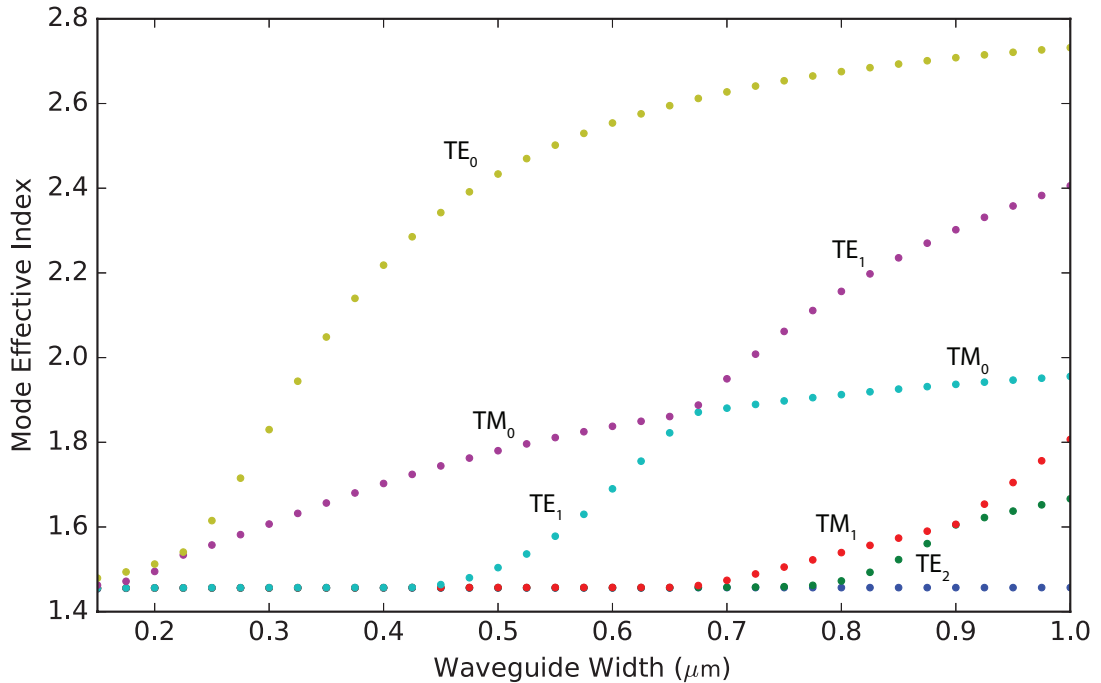


Figure 2.2: Mode effective indices for various widths of a 220 nm tall Si waveguide at 1550 nm. Effective index increases as width increases, pulling more field energy inside the waveguide core. Occasionally modes cross in index, for example near 675 nm for the TM_0 and TE_1 modes. This occurs again at 220 nm width where the waveguide switches from being wider than it is tall to vice-versa. Modes are cutoff at narrow widths (≈ 450 nm for TE_1) where they approach the bulk index of the cladding. Note that the effective index is most sensitive to changes in width for narrow widths and the TE_0 mode.

placement error in raster-scanned electron-beam lithography [29]. Some additional loss might also be introduced during etching, either from physical damage to the waveguide sidewall or from chemical contamination and dangling bonds created by reactive etch gases [30–32]. Regardless of the cause of the roughness, we can minimize its effect on optical scattering by using as wide a waveguide as possible, pulling light into the waveguide core and minimizing the amount of optical power at the sidewall.

Why, then, are waveguides usually not very wide? In most cases, we want waveguides to only support a single spatial mode per polarization. Very wide

waveguides begin to support multiple higher-order modes, each of which propagates with a different β . This modal dispersion corrupts high-speed data, and the simple existence of multiple modes complicates design of almost any useful device. Thus, we usually choose a waveguide that is as wide as possible while remaining single-mode, typically 450 nm wide for 220 nm-thick silicon or about 1 μm wide for 300 nm-thick silicon nitride for TE-polarized light (electric field in the plane of the wafer).

One compelling use for very narrow waveguides is the inverse taper for coupling between on-chip waveguides and optical fiber [33, 34]. Deliberately narrowing the waveguide to below about 200 nm causes the waveguide to lose confinement, expanding the mode to propagate primarily in the cladding. This large mode (approximately 2.5 μm $1/e^2$ diameter) matches well with the mode at the focus of a lensed fiber, allowing efficient coupling between the two.

2.2 Directional Couplers

The most basic stepping stone from single waveguides to more complex devices is a coupler, one that splits power between two waveguides in some designed ratio. With waveguides, couplers can be extremely straightforward—simply running two waveguides parallel to each other with a small oxide gap between them will couple light from one to the other. This coupling occurs because the waveguide modes have an exponentially-decaying evanescent field outside of the waveguide core that overlaps with the adjacent waveguide mode. By controlling the gap between the waveguides as well as the length that they run parallel, we control the ratio of coupling.

Much like the waveguide mode problem, closed-form models of the coupling problem are well-studied under the name of coupled mode theory [35, 36]. Power couples back and forth between the two waveguides as it propagates in z , with power in each waveguide varying as $\sin^2 z$. The period of that sine is set by the waveguide shape and gap, with larger mode overlap giving stronger coupling and a shorter period. For more exact simulations in practical use, we prefer computational methods that can properly account for the coupling in the entire structure, including bent sections of waveguide. Finite-difference time-domain (FDTD) simulations [37, 38], which solve the full electric and magnetic field vectors stepped in time, give robust solutions to this and other electromagnetism problems, but are computationally difficult and scale very poorly with problem size. Instead, we typically again exploit the mode description of the waveguides and use eigenmode expansion (EME) techniques for a reasonably fast simulation. Typical results for a directional coupler are shown in Figure 2.3.

Regardless of the coupler details, we can describe a black-box coupler as a device that, given two input fields E_1, E_4 and two output fields E_2, E_3 , transforms the inputs to the outputs via a 2x2 matrix [39, 40]:

$$\begin{bmatrix} E_2 \\ E_3 \end{bmatrix} = \begin{bmatrix} t & i\kappa \\ i\kappa & t \end{bmatrix} \begin{bmatrix} E_1 \\ E_4 \end{bmatrix} \quad (2.3)$$

For a lossless coupler we additionally impose from conservation of energy:

$$t^2 + \kappa^2 = 1 \quad (2.4)$$

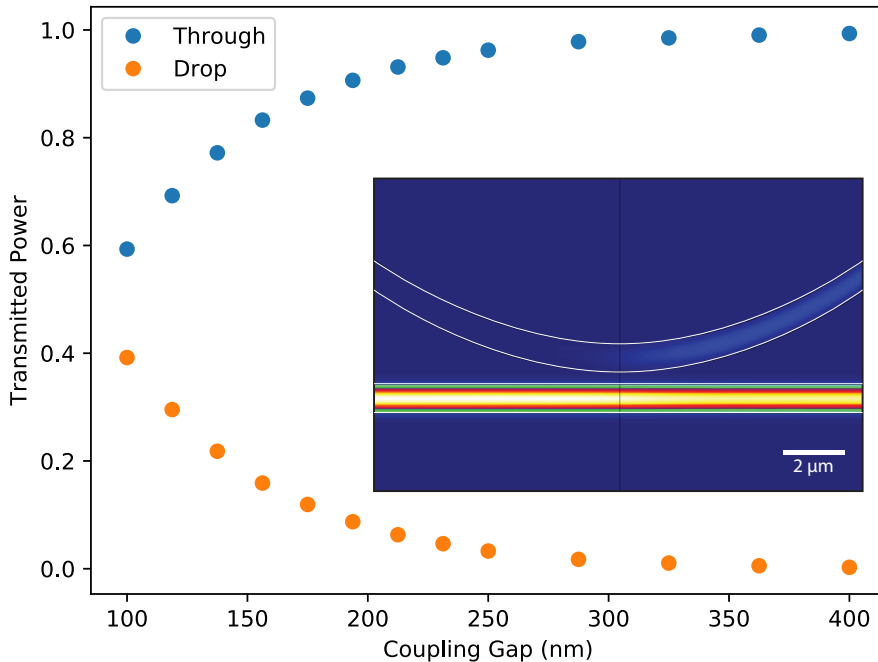


Figure 2.3: Eigenmode expansion directional coupler simulations. For a silicon waveguide directional coupler with one straight waveguide and one curved waveguide with a bend radius of $25 \mu\text{m}$, coupling ratios vary between 40% power transferred to the second waveguide drop port at a 100 nm gap to 0.26% at a 400 nm gap. Inset: propagating power for a directional coupler with a 200 nm gap, corresponding to a coupling ratio of 7.9%. The image is distorted to emphasize the waveguide curvature; the scale bar corresponds to the horizontal direction.

From a system perspective we can then describe the entire coupler with a single parameter t between 0 and 1.

2.3 Ring Resonators

Taking a coupler and connecting one of its output ports back onto its own input forms one of the most pervasive structures in silicon photonics: a ring resonator. Light launched into one port of the directional coupler will propagate around the ring many times, making the resonator exceedingly sensitive to small changes in the

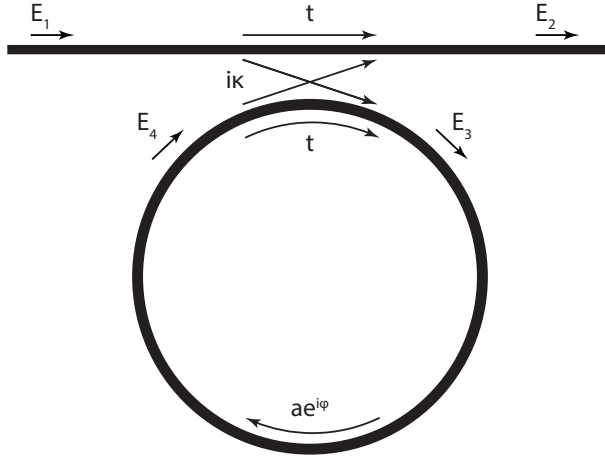


Figure 2.4: Theoretical model of a waveguide-coupled ring resonator.

ring. This sensitivity makes ring resonators useful for a wide range of applications, including sensors [41–44], efficient electro-optic modulators [5, 45], wavelength-selective filters [46, 47], low-power switches [48–50], low-threshold lasers [51–54], and nonlinear optics [55–57].

The ring resonator’s functionality hinges on interference in the directional coupler. Light propagating around the ring interferes with new light entering from the input waveguide, causing the power in the output waveguide to be strongly dependent on the input wavelength or the loss and phase of the ring waveguide. Mathematically, we can model the ring (Figure 2.4) by combining equations 2.3 and 2.4 with an additional one describing the loss a and phase $\phi = \beta L$ picked up in one round-trip pass of the ring:

$$E_4 = ae^{i\phi} E_3 \tag{2.5}$$

A small amount of algebra yields:

$$E_2 = \frac{t - ae^{i\phi}}{1 - ate^{i\phi}} E_1 \quad (2.6)$$

On-resonance ($\phi = 2\pi m$ for integer m , equivalent to an integer number of wavelengths fitting around the ring), the light interferes constructively in the ring and destructively in the output port. Transmission on-resonance is the extinction of this destructive interference, only dependent on the round-trip loss and coupling strength:

$$T = \left(\frac{E_2}{E_1} \right)^2 = \left(\frac{t - a}{1 - at} \right)^2 \quad (2.7)$$

Transmission on-resonance has a minimum where $a = t$, a condition known as critical coupling. Rings with $a > t$ (equivalently, $a < \kappa$) are overcoupled, since coupling into the ring exceeds the amount necessary to replenish the round-trip loss. Similarly, $a < t$ or $a > \kappa$ describes an undercoupled ring. Transmission curves of rings for various coupling conditions are plotted in Figure 2.5

From this spectrum¹ it is possible to extract a resonance full-width at half-maximum [58]:

$$\text{FWHM} = \frac{(1 - at)\lambda_0}{\pi n_g L \sqrt{at}} \quad (2.8)$$

n_g is the waveguide group index, which takes into account the change of the effective index versus wavelength:

$$n_g = n_{\text{eff}} - \lambda_0 \frac{\partial n_{\text{eff}}}{\partial \lambda_0} \quad (2.9)$$

¹Truly a spectrum, since ϕ is equivalent to wavelength via $\phi = 2\pi n_g L / \lambda$.

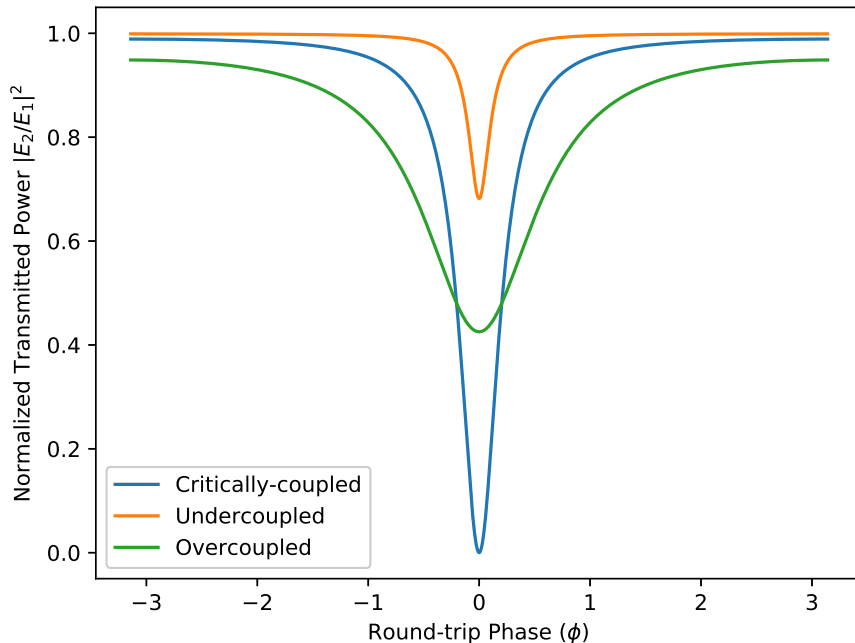


Figure 2.5: Ring transmission versus round-trip phase for $a = 0.9$ and three values of t : $t = 0.9$ (critically-coupled), $t = 0.99$ (undercoupled) and $t = 0.6$ (overcoupled).

We define the quality factor Q of the resonance as a ratio of the frequency f to the linewidth Δf :

$$Q \equiv \frac{f}{\Delta f} = \omega\tau = \frac{\lambda_0}{\Delta\lambda} - \frac{\Delta\lambda}{4\lambda_0} \approx \frac{\lambda_0}{\Delta\lambda} \quad (2.10)$$

where the approximation holds for spectral linewidth much smaller than the resonant wavelength ($\Delta\lambda \ll \lambda_0$). Q factor can also be measured in the temporal domain; it is directly proportional to the exponential lifetime τ of a photon in the ring. Typical Q factors in integrated ring resonators are on the order of thousands to millions, corresponding to photon lifetimes from tens of picoseconds to several nanoseconds.

Combining 2.8 and 2.10, we find expressions for the quality factor in terms of the ring loss and coupling coefficient:

$$Q_L = \frac{\pi n_g L \sqrt{at}}{(1 - at)\lambda_0} \quad (2.11)$$

$$Q_i = \frac{\pi n_g L \sqrt{a}}{(1 - a)\lambda_0} \quad (2.12)$$

Q_L is the loaded quality factor, while Q_i is the intrinsic quality factor ($t = 1$). Loaded quality factors include the effective ring loss induced by out-coupling, while intrinsic quality factors describe just the loss in the ring itself. For critically-coupled ($a = t$), high-Q ($a \rightarrow 1$) rings:

$$\frac{Q_i}{Q_L} = \frac{\sqrt{a}}{1 + a} \approx \frac{1}{2} \quad (2.13)$$

Relating round-trip loss to the power attenuation coefficient per unit length and an obscure though convenient approximation allows us to extract a simple expression for intrinsic Q valid for $a \rightarrow 1$ [59]:

$$a = e^{-\alpha L/2} \quad (2.14)$$

$$\frac{1 - a}{\sqrt{a}} \approx -\ln a = \frac{\alpha L}{2} \quad (2.15)$$

$$Q_i \approx \frac{2\pi n_g}{\alpha \lambda_0} \quad (2.16)$$

The equation can be simplified even further by using the complex effective index $\tilde{n}_{\text{eff}} = n_{\text{eff}} + ik_{\text{eff}}$, in which case:

$$\alpha = \frac{2\pi k_{\text{eff}}}{\lambda_0} \quad (2.17)$$

$$Q_i \approx \frac{n_g}{k_{\text{eff}}} \quad (2.18)$$

A few additional values describe the full behavior of a ring resonator. The free spectral range, first, is the distance in wavelength between adjacent resonances:

$$FSR = \frac{\lambda^2}{n_g L} \quad (2.19)$$

The effective selectivity of the filter can then be described as the ratio of free spectral range and resonance width, called finesse:

$$\mathcal{F} \equiv \frac{FSR}{\Delta\lambda} = \frac{Q\lambda}{n_g L} = \frac{\pi\sqrt{at}}{1-at} \approx \frac{-\pi}{\ln at} \quad (2.20)$$

The behavior of ring resonators is surprisingly rich for such a simple system, and this theoretical formulation enables the straightforward design of a wide variety of photonic devices.

2.4 Fourier Optics for Optical Phased Arrays

Wafer-scale fabrication and advanced lithography enable almost effortless manufacturing of photonic components by the thousands. While such manufacturing is easily brought to bear to reduce costs of simple components, it is perhaps most powerful in building large collections of devices that work together. In electronics,

large-scale microprocessors and VLSI circuits are far more powerful than single cheap transistors. One of the most promising applications for large-scale photonics is the optical phased array, a solid-state beamforming system that projects arbitrary light patterns by controlling the phase front of the output light.

The key theoretical problem in optical phased arrays is to convert an arbitrary phase and amplitude profile in the near-field (at the chip facet) to a amplitude profile in the far-field (at the target, far away from the chip). In general, solving this system seems to require a full solution of Maxwell's equations, which is analytically tricky and computationally infeasible. Conveniently, though, light propagation through phase-distorting elements is a key problem in traditional optics, which has developed the theory of Fourier optics to easily treat these situations [60]. Since our phased arrays deal with beam formation at very wide-angles off-axis, we develop here a non-paraxial formation of Fourier optics, valid for the Fraunhofer far-field:

$$R \gg \frac{W^2}{\lambda} \quad (2.21)$$

where W is the size of the phased-array aperture and R is the distance at which we measure the diffraction pattern.

We begin with a plane of arbitrary sources in the $x' - y'$ plane at $z = 0$ and solve for its propagation into $z > 0$ to a point (x, y, z) (Figure 2.6). This is basically the problem of diffraction from an aperture and is solved exactly by the Rayleigh-Sommerfeld diffraction theory [61, 62]:

$$E_{x,y}(x, y, z) = \iint_A dx' dy' E_{x,y}(x', y', 0) \frac{e^{-ikR_1}}{2\pi R_1} \left(ik + \frac{1}{R_1} \right) \frac{z}{R_1} \quad (2.22)$$

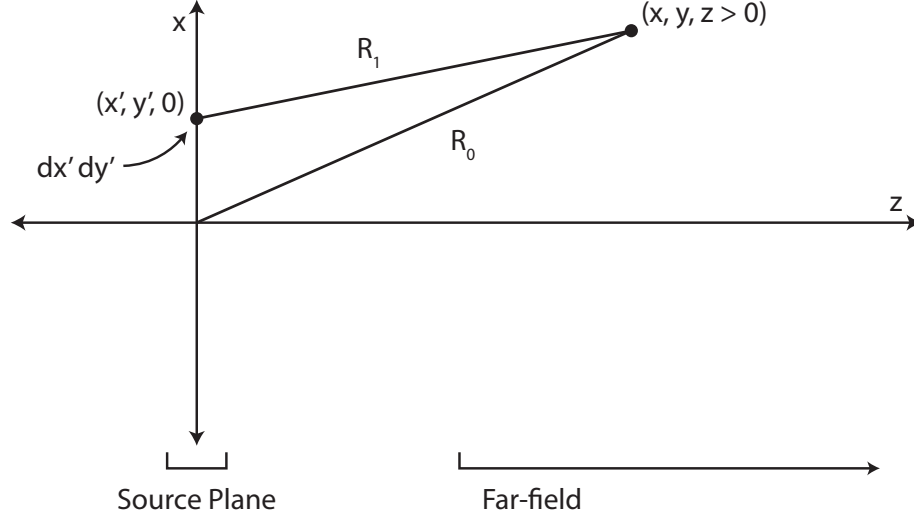


Figure 2.6: Geometry for Fourier optics derivation. A distributed source at the $z = 0$ plane diffracts into the right half-space, solved at a point (x, y, z) .

$$E_z(x, y, z) = \iint_A dx' dy' \frac{e^{-ikR_1}}{2\pi R_1} \left(ik + \frac{1}{R_1} \right) \left[E_x(x', y', 0) \frac{x' - x}{R_1} + E_y(x', y', 0) \frac{y' - y}{R_1} \right] \quad (2.23)$$

where $k = 2\pi/\lambda_0$ is the wavenumber and R_1 is the distance from an infinitesimal emitter to the point of interest, and the integral is over the emitting aperture. We are interested in the far-field solution, where R_1 is very large. Therefore, we can approximate $R_1 \rightarrow R_0$, where R_0 is the distance from the origin, except in the phase term e^{ikR_1} . We can safely approximate the amplitude terms because errors in the final solution are only on the order of the error in the approximation; however, the phase term must be accurate to $\ll \pi$ regardless of the magnitude of R to correctly model interference effects. Thus, $ik = i2\pi/\lambda \gg 1/R_1$, $x' \ll x$, and $y' \ll y$, giving:

$$E_{x,y}(x, y, z) = \frac{ik}{2\pi R_0} \frac{z}{R_0} \iint_A dx' dy' E_{x,y}(x', y', 0) e^{-ikR_1} \quad (2.24)$$

$$E_z(x, y, z) = \frac{ik}{2\pi R_0} \frac{1}{R_0} \iint_A dx' dy' [xE_x(x', y', 0) + yE_y(x', y', 0)] e^{-ikR_1} \quad (2.25)$$

In the phase term, for $R_0 \gg 2x'^2/\lambda$ and $R_0 \gg 2y'^2/\lambda$:

$$R_1 = [(x - x')^2 + (y - y')^2 + (z - 0)^2]^{1/2} \approx R_0 - \frac{xx' + yy'}{R_0} \quad (2.26)$$

$$E_{x,y}(x, y, z) = \frac{ie^{-ikR_0}}{\lambda R_0} \frac{z}{R_0} \iint_A dx' dy' E_{x,y}(x', y', 0) \exp\left(i2\pi \left[\left(\frac{x}{\lambda R_0}\right) x' + \left(\frac{y}{\lambda R_0}\right) y'\right]\right) \quad (2.27)$$

$$E_z(x, y, z) = \frac{ie^{-ikR_0}}{\lambda R_0} \frac{1}{R_0} \iint_A dx' dy' [xE_x(x', y', 0) + yE_y(x', y', 0)] \exp\left(i2\pi \left[\left(\frac{x}{\lambda R_0}\right) x' + \left(\frac{y}{\lambda R_0}\right) y'\right]\right) \quad (2.28)$$

These equations are simply Fourier transforms on the spatial frequencies of the emitter:

$$f_x = \frac{-x}{\lambda R_0}, \quad f_y = \frac{-y}{\lambda R_0} \quad (2.29)$$

$$E_{x,y}(x, y, z) = \frac{ie^{-ikR_0}}{\lambda R_0} \frac{z}{R_0} \hat{E}_{x,y} \quad (2.30)$$

$$E_z(x, y, z) = \frac{-ie^{-ikR_0}}{\lambda R_0} \frac{1}{R_0} [x\hat{E}_x + y\hat{E}_y] \quad (2.31)$$

Note that in this non-paraxial case, even light that emits from the phased array perfectly polarized (purely E_x , for example) can have significant energy in the longitudinal (E_z) field component off-axis. A similar phenomenon occurs for high-numerical aperture (non-paraxial) focusing of Gaussian beams [63].

This idea of diffraction as a Fourier transform makes several key results from phased arrays intuitive. We can imagine the phased array as a series of point emitters arranged in a rectangular aperture—that is, a comb multiplied by a box function. Taking the Fourier transform gives the Fourier transform of the comb convolved with the Fourier transform of the box. A box of dimension W_x by W_y , solving equation 2.27, becomes in the far field:

$$E_x(x, y, z) = \frac{ie^{-ikR_0}}{\lambda R_0} \frac{z}{R_0} W_x W_y \operatorname{sinc}\left(\frac{\pi x W_x}{\lambda R_0}\right) \operatorname{sinc}\left(\frac{\pi y W_y}{\lambda R_0}\right) \quad (2.32)$$

This is the well-known sinc pattern from single-slit diffraction. In spherical coordinates and intensity units:

$$I(\theta, \Phi) = I_0 \operatorname{sinc}^2\left(\frac{\pi W_x}{\lambda} \sin \theta\right) \operatorname{sinc}^2\left(\frac{\pi W_y}{\lambda} \sin \Phi\right) \quad (2.33)$$

The near-field comb becomes a far-field comb as well, with angular spacing:

$$\theta = \arcsin \frac{\lambda}{2d} \quad (2.34)$$

where d is the spacing between emitters in the phased array. The end result, convolving this comb with equation 2.33, is a series of sinc-like beams (each with its own tails of sidelobes) spaced in periodic grating lobes. Because real emitters are not isotropic point emitters but rather have some spread, this entire function

is then multiplied by an envelope emitter factor, attenuating grating lobes away from $\theta = 0^\circ$ [64].

CHAPTER 3

GRAPHENE RING MODULATOR

3.1 Device Concept

Graphene has generated exceptional interest as an optoelectronic material [65, 66] because its high carrier mobility [11, 12] and broadband absorption [67] promise to make extremely fast and broadband electro-optic devices possible [14, 15, 68, 69]. Electro-optic graphene modulators reported to date, however, have been limited in bandwidth to a few GHz [70–75] because of the large capacitance required to achieve reasonable voltage swings. Here we demonstrate a graphene electro-optic modulator based on resonator loss modulation at critical coupling [76] that shows drastically increased speed and efficiency. Our device operates with a 30 GHz bandwidth and with a state-of-the-art modulation efficiency of 15 dB per 10 V. We also show the first high-speed large-signal operation in a graphene modulator, paving the way for fast digital communications using this platform. The modulator uniquely uses silicon nitride waveguides, an otherwise completely passive material platform, with promising applications for ultra-low-loss broadband structures and nonlinear optics.

Integrated graphene modulators to date, by nature of their electroabsorptive structure, carry fundamental tradeoffs between speed and efficiency. In these structures, graphene forms at least one electrode of a large capacitor; a voltage applied to this capacitor causes carriers to accumulate on the graphene sheet and gates the interband absorption of the graphene through Pauli blocking [77]. This change in absorption modulates the intensity of light traveling through the waveguide. Operation speed can be increased by using a thicker gate oxide, but the lower ca-

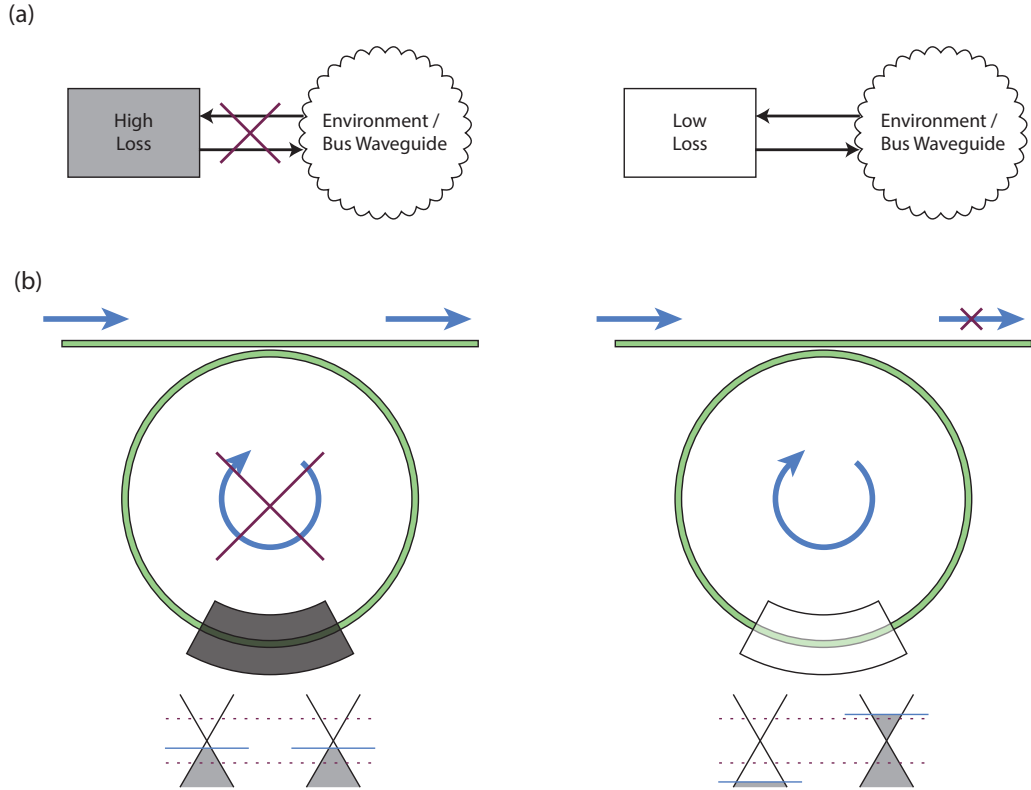


Figure 3.1: Critical coupling effect and device concept. **a.** Schematic concept. For a given coupling strength, a low-loss system will be more coupled to its environment than a high-loss system because of impedance matching. A resonator designed for critical coupling at low intrinsic losses would thus be undercoupled at high losses. **b.** Effect in a graphene-clad ring resonator and band diagrams for the two gated sheets of graphene in the parallel-plate capacitor structure. When a graphene section with high loss is integrated with a ring resonator, it prevents light from circulating in the cavity, leading to high transmission through the bus waveguide. When electrostatically doped, the graphene becomes transparent, allowing light to circulate in the cavity and causing low transmission through the bus waveguide.

capacitance makes for a lower carrier concentration change with voltage and reduced efficiency.

We overcome this tradeoff by exploiting critical coupling effects, in which an increase in loss in a coupled resonator increases the system transmission by changing the condition for resonator coupling (Figure 3.1a). We design a resonator

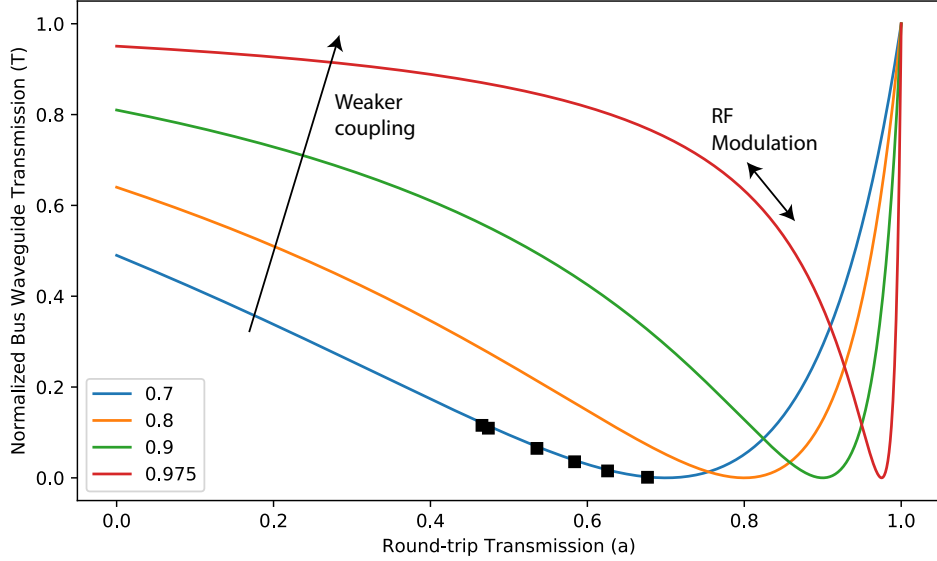


Figure 3.2: Theoretical transmission on-resonance ($\phi = 0$), neglecting graphene phase modulation effects, for $t = \{0.7, 0.8, 0.9, 0.975\}$. Black squares indicate the operating points of our experimental device, which has $t = 0.70$. Note that lower losses in the ring resonator would permit devices with lower insertion loss and higher transmission slopes.

to be critically coupled for low losses. When losses are increased, the resonator then becomes undercoupled, increasing transmission through the bus waveguide. This effect has been used to create sensitive all-optical switches [76, 78]. Here, we use a silicon nitride ring resonator above a portion of which we integrate a graphene/graphene capacitor to modulate the round-trip ring loss (Figure 3.1b). At 0 V bias, both graphene sheets in the capacitor are lightly doped and thus opaque, so the ring has high loss and is undercoupled to the bus waveguide. Applying a voltage to the capacitor dopes the graphene sheets heavily, causing their absorption to decrease as the Fermi level crosses half the incident photon energy. The ring, now substantially lower-loss, couples to the bus waveguide, decreasing the systems transmission, as predicted theoretically [79].

Sensitivity to ring loss and on-state insertion loss can be designed by choosing the ring-waveguide coupling constant. In Figure 3.2, we plot equation 2.7, where each contour represents a graphene ring modulator with a designed ring-waveguide coupling coefficient t . Changing round-trip loss a by applying a bias or RF voltage moves along this curve. We can choose the bias point loss and t arbitrarily for a tradeoff between insertion loss ($1 - T$) and voltage sensitivity ($\partial T/\partial a \cdot \partial a/\partial V$). Operating near critical coupling gives the best sensitivity of the modulator but the worst insertion loss.

We note that this mechanism is not simply ring-enhanced absorption modulation, as the ring has little circulating power when the graphene is lossiest, and the modulator has the least transmission when the graphene is nominally transparent. Instead, attenuation occurs via destructive interference at the coupling region, and this interference is modified by the voltage-controlled ring loss. This destructive interference is significantly more sensitive to changes in loss than an electroabsorption modulator.

3.2 Design and Fabrication

We demonstrate this interference effect by integrating graphene over a ring resonator fabricated from low-temperature plasma-enhanced chemical vapor deposition (PECVD) silicon nitride [80] (Figure 3.3). In contrast to previously demonstrated graphene integration on silicon waveguides, which have relatively high loss and a limited transparency window, silicon nitride has ultra-low loss and broad transparency, enabling nonlinear and quantum systems. Low-temperature deposition of silicon nitride also allows integration on the CMOS backend [9] or even on

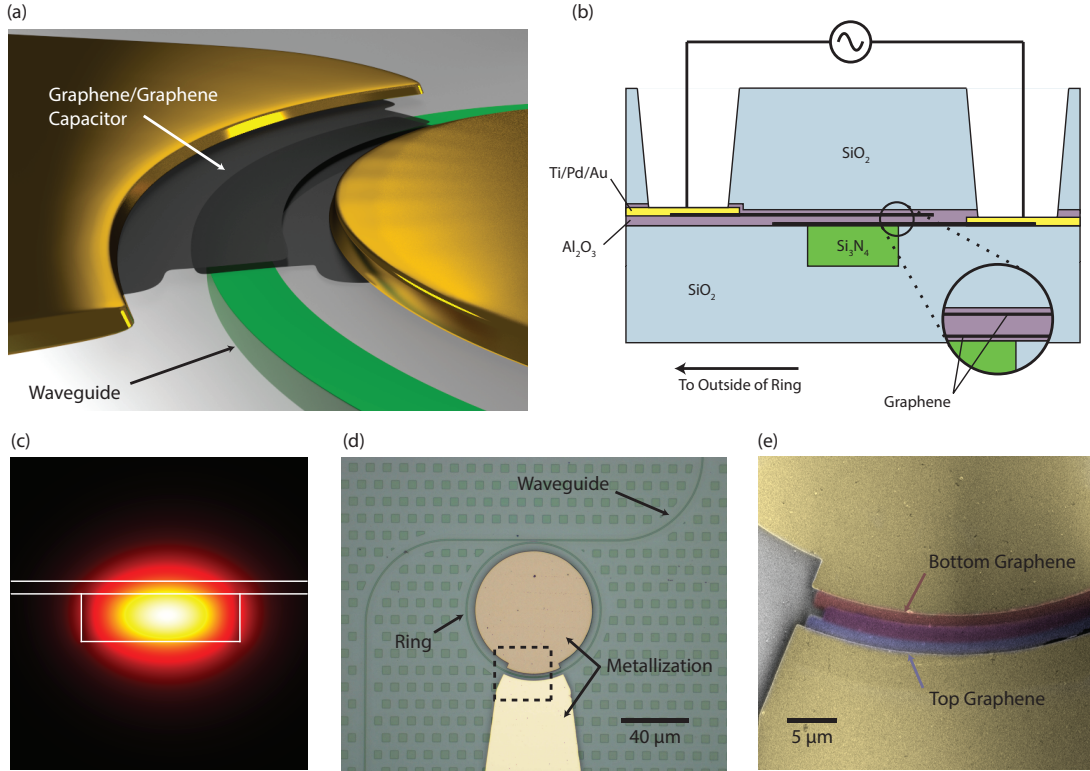


Figure 3.3: Device Design. **a.** Schematic of the modulator consisting of a graphene/graphene capacitor integrated along a ring resonator. **b.** Cross-section of the device. Two layers of graphene separated by a 65 nm interlayer Al_2O_3 dielectric form a parallel-plate capacitor. **c.** TE mode Poynting vector showing boundaries of silicon nitride and Al_2O_3 . The waveguide mode overlaps both graphene sheets. **d.** Optical micrograph showing bus waveguide, ring resonator, and Ti/Pd/Au metallization. Green squares are chemical mechanical planarization fill pattern. Scale bar, 40 μm . **e.** False-color SEM of dashed area in (d). Top and bottom graphene layers (blue and red) overlap in a 1.5 by 30 μm section over the buried ring waveguide. Gold areas indicate metal contacts. Scale bar, 5 μm .

flexible substrates [81]. We use a waveguide cross section 1 μm wide by 300 nm tall to guide single-mode TE light. This waveguide forms a ring resonator with radius 40 μm and bus waveguide coupling gap between 200 nm and 900 nm. On top of a portion of the ring resonator we fabricate a graphene/graphene capacitor consisting of two sheets of monolayer graphene grown via chemical vapor deposition (CVD) on copper foil [82] and wet-transferred to the waveguide substrate. Approximately 65 nm of atomic layer deposition (ALD) Al_2O_3 forms the interlayer

dielectric. The dielectric is five to ten times thicker than previous work [70,71], reducing capacitance and allowing our modulator to operate at much higher speeds. The capacitor forms an arc along the silicon nitride ring with 30 μm optical path length and 1.5 μm width overlap between the two layers. The graphene is completely encapsulated in Al_2O_3 , providing an electrically insulating environment free from environmental effects or surface doping.

3.2.1 Graphene Transfer

Graphene transfer and patterning over waveguides is not a trivial process. Many of our processing steps were inspired by [83]. Typically, starting from as-grown graphene on thin copper foil, we begin by spinning a layer of polymethyl methacrylate (PMMA), letting that layer dry, and then removing the copper foil by floating the sample in ferric chloride ($FeCl_3$) etchant solution. The PMMA serves as a handle to maintain the integrity of the graphene layer through handling. We then rinse the copper etchant off in a series of deionized water baths, transferring from bath to bath by scooping the graphene with a silicon wafer or glass slide. Some metallic contamination remains from either the copper foil or the $FeCl_3$ solution, which we remove by SC2 solution (HCl and H_2O_2 in water), which is typically used before furnace processing to remove metallic contaminants. SC2 is usually mixed 1:1:6 $HCl:H_2O_2:H_2O$ by volume, but we use a weaker 1:1:20 ratio to avoid attacking the graphene or the PMMA handle. Some groups also suggest a SC1 clean ($NH_4OH:H_2O_2:H_2O$) to remove non-graphene organic contamination, but we find that this attacks the graphene itself and generates gas bubbles under the sheet that are hard to remove and will break the graphene during later transfer steps.

Clean graphene can generally be scooped onto the final substrate (immersing the wafer with waveguides into the water bath), but in our case there is an extra complication because of the Al_2O_3 layer deposited before the graphene transfer. Alumina is quite hydrophobic as-grown, and wet-transferred graphene has a sheet of water underneath it—the graphene tends to curl up on itself as the drying water beads up on the hydrophobic film. We can make the alumina hydrophilic by treating it with piranha solution ($\text{H}_2\text{SO}_4:\text{H}_2\text{O}_2$), available as Cyantek Nanostrip, which hydrogen-terminates the surface. The graphene then is stretched out by the evaporating water as it sheets across the wafer, yielding a wrinkle-free transfer. After squeezing out most of the water with a gentle nitrogen flow directly normal to the wafer surface, we leave the graphene to air dry, then bake at $145\text{ }^\circ\text{C}$, above the glass transition temperature of the PMMA, to relax wrinkles in the polymer overcoat. After stripping the PMMA in acetone, we bake again at $170\text{ }^\circ\text{C}$ to adhere the graphene strongly to the substrate [83]. Raman spectroscopy (Figure 3.4) both confirms the defect-free, monolayer quality of the graphene sheet and tells us (from the positions of the peaks [84]) that the graphene is strongly p-doped from the acidic transfer process.

3.2.2 Surface Planarization

The waveguide topography on top of which the graphene is placed poses further challenges. Graphene forms bridges over the 300 nm waveguide steps (Figure 3.5). When the water underneath dries, surface tension pulls the graphene into the bottom corner of the waveguide, breaking it. This makes the material electrically discontinuous and also hampers careful patterning. We circumvent this issue by planarizing the waveguides via chemical mechanical planarization (CMP) prior to

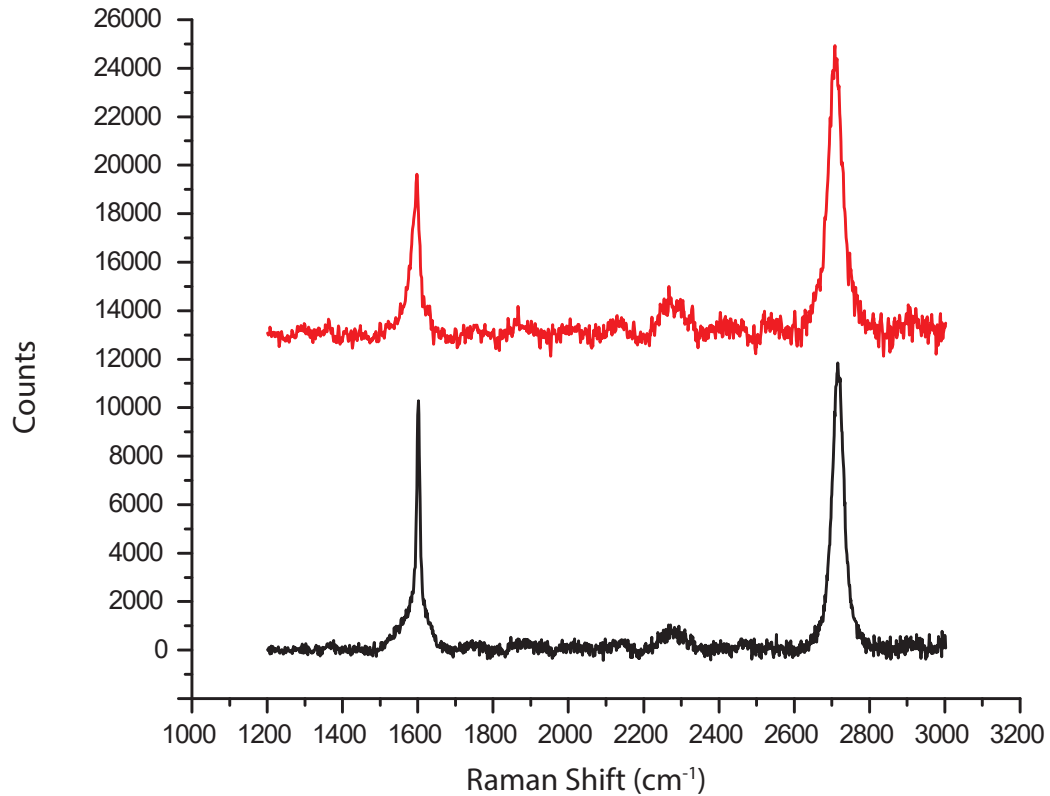


Figure 3.4: Raman spectra for bottom (black) and top (red) layer of graphene, with 514 nm excitation. Baseline photoluminescence from other materials has been subtracted. G peaks are at 1601 and 1597 cm^{-1} and 2D peaks at 2717 and 2708 cm^{-1} , respectively. These peak positions indicate a p-type doping of approximately $5 \times 10^{12} \text{ cm}^{-2}$.

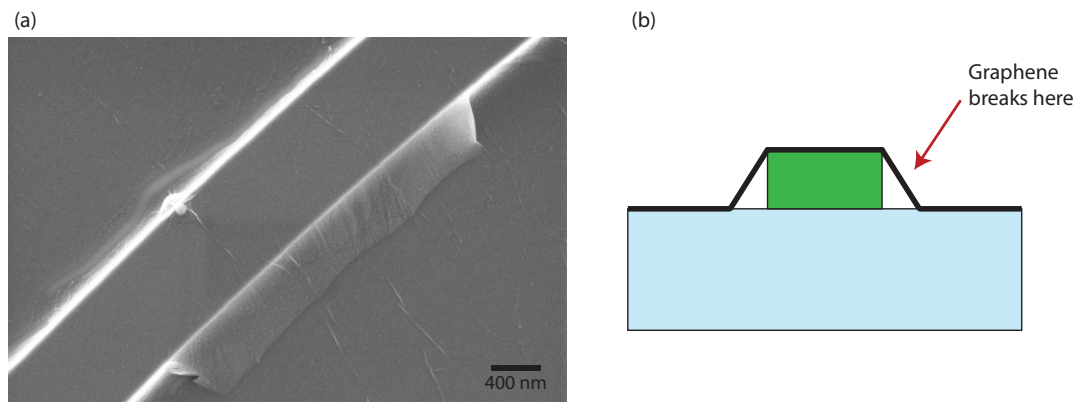


Figure 3.5: Graphene bridging over waveguide topography. **a.** Scanning electron micrograph of broken suspended graphene over a SiN waveguide. **b.** Schematic of graphene bridging over underlying step.

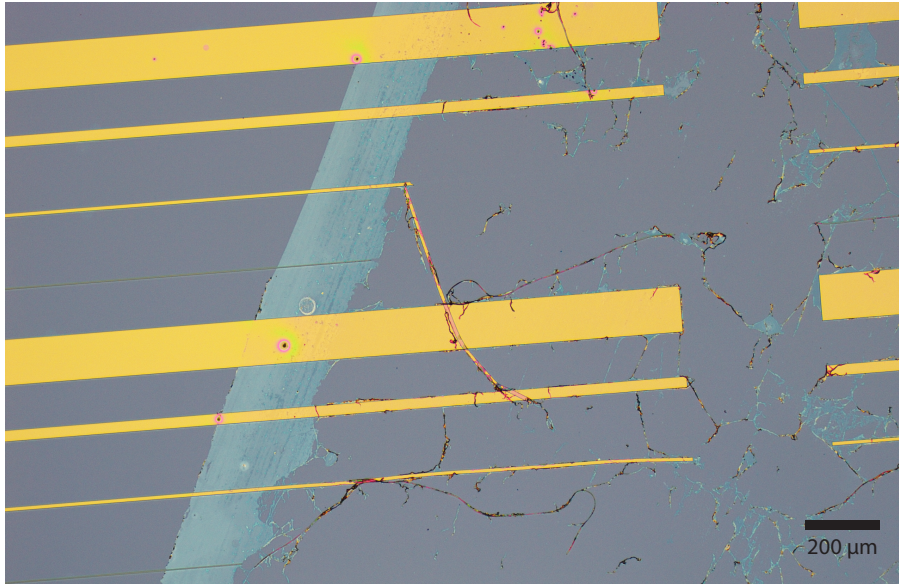


Figure 3.6: A failed patterning of Dow UV210-0.6 resist directly on graphene. The resist adheres to the alumina on the left side but not to the graphene on the right.

transfer. Filling with SiO_2 and back-polishing provides a flat surface at the top of the waveguide onto which graphene easily transfers. Stopping the polishing on the top surface of the silicon nitride is key to preserve the optical performance of the waveguide. Conveniently, polishing oxide back to stop on a nitride layer is identical to shallow trench isolation (STI) in CMOS processes, and slurries (Dow Celexis CX94S, consisting of cerium oxide nanoparticles) are available that polish oxide selectively to nitride. Periodic CMP fill squares ($5 \times 5 \mu\text{m}$ on $10 \mu\text{m}$ pitch) provide an even surface for the CMP pad to push on and stop at; without this fill pattern even the selective slurry will polish the nitride off because the pad force is concentrated on just those small isolated features.

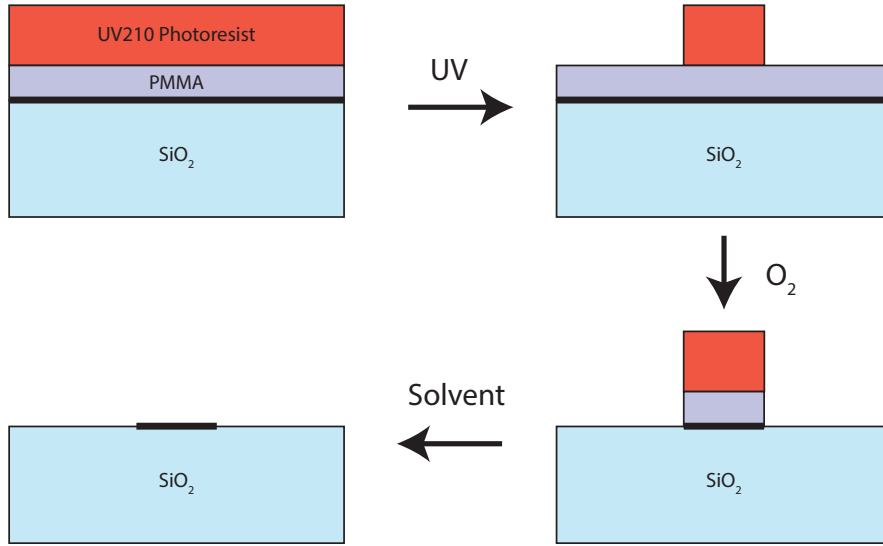


Figure 3.7: Schematic of bilayer resist graphene patterning process. We spin UV210 deep-UV photoresist on top of a PMMA underlayer, expose and develop the photoresist, then etch both the PMMA and graphene in oxygen plasma.

3.2.3 Deep-UV Lithography and Patterning

We use deep-UV lithography (248 nm, NA=0.63 stepper, ASML PAS 5500/300C) to pattern both the waveguides and graphene. In addition to drastically reduced turn-around time compared to electron-beam lithography, the stepper has <50 nm alignment tolerances, key for the overlay of the top and bottom graphene capacitors. Problematically, deep-UV resist does not adhere well to graphene, which has very weak bonding out of the atomic plane (Figure 3.6). Usually, an anti-reflective coating is spun on between the resist and the substrate as an adhesion promoter, but ARC can only be removed in strong oxidizers (O_2 plasma or piranha solution), which would damage the underlying graphene. Not all resists have difficulty adhering to graphene—PMMA, for example, adheres quite strongly to graphene. Unfortunately, it is extremely insensitive to DUV light, with exposure times measured in hours. We can combine the photoactivity of UV210 resist

with the adhesion of PMMA, however, by employing a bilayer resist process. We first spin and bake PMMA on the graphene, then spin and bake UV210 on top of it. After exposing the UV210, we use oxygen plasma to pattern both the PMMA and the underlying graphene, then strip the entire stack in Dow Remover 1165 (N-methyl-2-pyrrolidone) (Figure 3.7). This double-spin process works because the resists use orthogonal solvents (anisole for PMMA and ethyl lactate for UV210) and bake times (170 °C for PMMA and 135 °C for UV210). Thus the PMMA layer remains unharmed by the spin and bake cycle of the UV210 and the resists form clean layers without intermixing. The final result of repeating this process for two layers of graphene is shown in Figure 3.8.

3.2.4 Metal-Graphene Contacts

The final challenge for fabricating high-speed graphene devices is creating low-resistance contacts. Metal-graphene contacts are extremely sensitive to contamination on the graphene surface that blocks electron flow. Evaporating metal via standard lift-off techniques tends to perform poorly because photoresist or lift-off underlayers (Microchem LOR) leave behind residues that block electron conduction between the metal and graphene. A number of groups have attempted to clean this residue via UV/Ozone treatment [85, 86], oxygen plasma [87], and thermal annealing [88]. We adopt a much better technique, however, which is to protect the graphene sheet with a deposited Al_2O_3 layer before contact photolithography, then selectively remove the protective film immediately before metal deposition [89]. Thus the graphene is never exposed to organic contamination after the initial PMMA-mediated transfer process. A cleaner transfer method, using either alternative polymers [90] or no polymer at all [91–93] could further improve

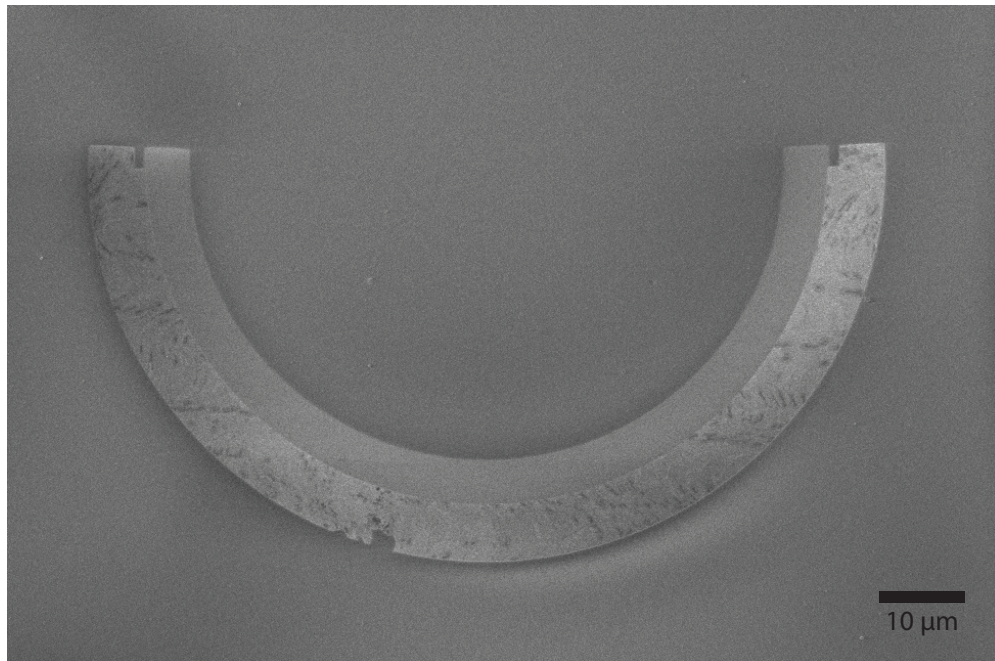


Figure 3.8: Scanning electron micrograph of two layers of transferred and patterned graphene, separated by a 65 nm Al₂O₃ dielectric. The outer semicircle is the top layer. The bottom graphene layer is unexpectedly still visible even though it is buried beneath the Al₂O₃ layer. Its visibility is strongly dependent on scan integration time, with the graphene disappearing at slow scan rates. We believe it is visible because of non-equilibrium charging as the electron beam penetrates through the alumina and induces short-lived charges in the conductive graphene layer.

the graphene cleanliness and both sheet and contact resistance. Further, there is increasing evidence that metal-graphene contact occurs best at the edge of the graphene sheet (where strong bonds are available), rather than through the surface. Modifying the process for such "edge contacts" [94–96] could dramatically increase the operation speed of the modulator.

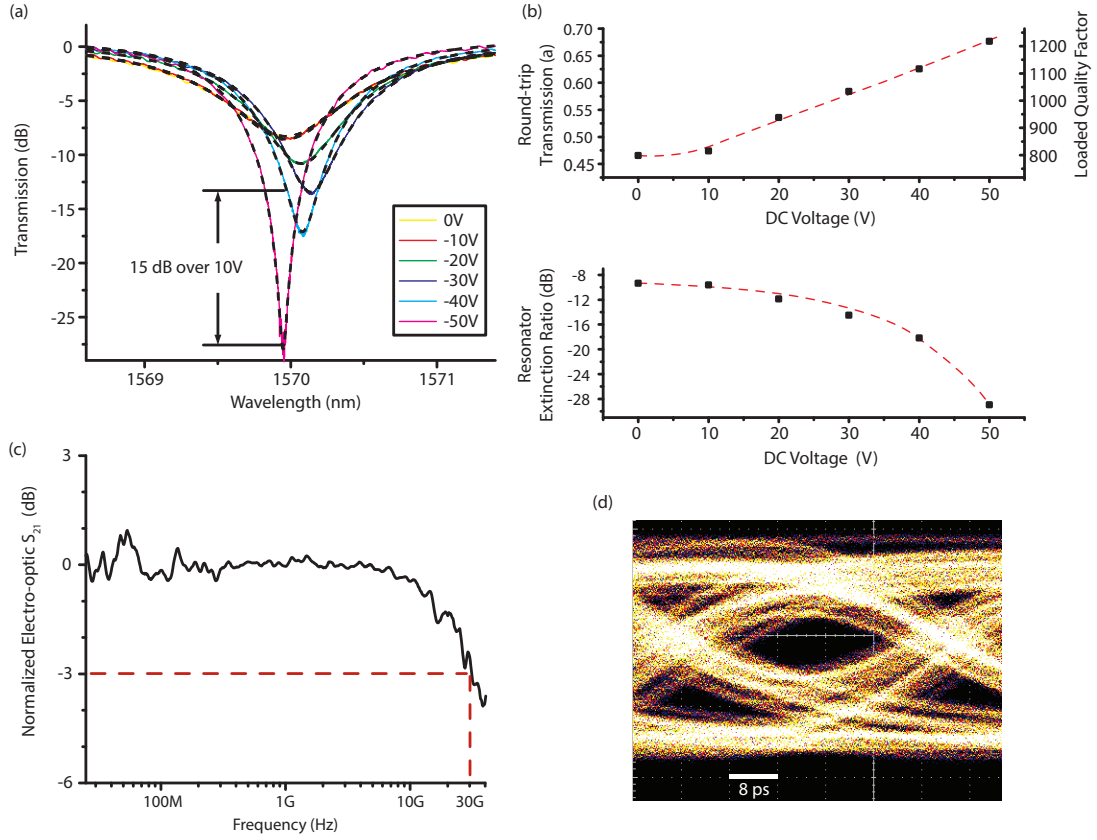


Figure 3.9: Electrical Response. **a.** Transmission spectra (colors) and theoretical curves (dashed black) for various applied DC voltages on a resonator with 300 nm gap between ring and bus waveguide. The ring resonance sharpens and becomes critically-coupled for higher voltages, corresponding to lower losses in the graphene. **b.** Ring round-trip transmission, loaded quality factor, and extinction ratio as a function of voltage, extracted from in (a). All theoretical curves share the same values for off-resonance optical power ($2.95 \mu\text{W}$) and ring-waveguide coupling constant $t = 0.7$. The dashed lines serve as a guide to the eye. **c.** Electro-optic S_{21} frequency response. The device displays clear RC-limited behavior with 30 GHz bandwidth. **d.** Open 22 Gbps 2^7-1 pseudo-random binary sequence non-return-to-zero eye diagram, measured at 7.5 V pk-pk and -30 V DC bias.

3.3 Measurements and Analysis

3.3.1 DC Measurements

We show the ability to tune the cavity transmission over 15 dB with 10 V swing (Figure 3.9a). Increasing the voltage (and thus decreasing the absorption in the

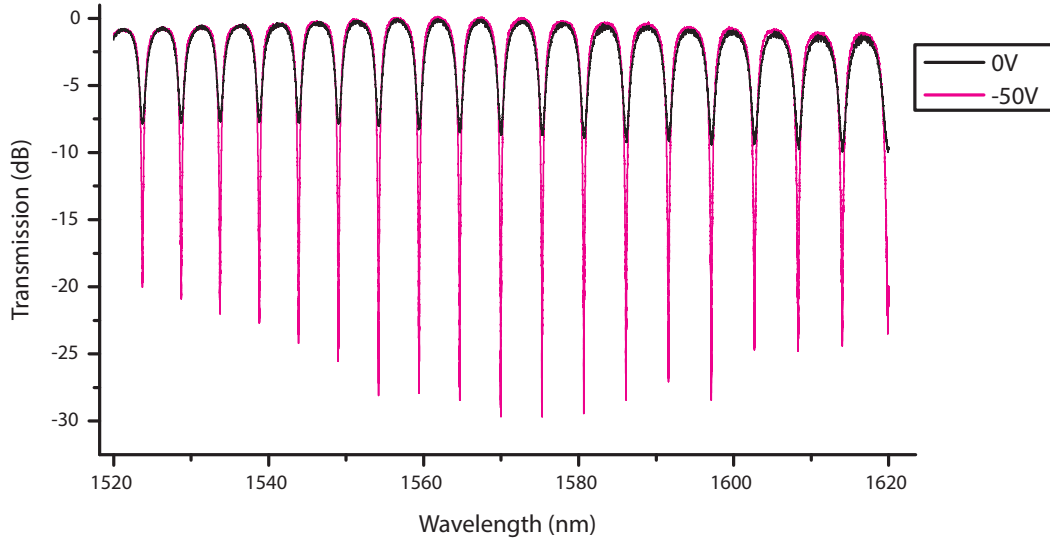


Figure 3.10: Transmission spectrum of the device from 1520 nm to 1620 nm, for 0 V (black) and -50 V (pink) DC bias. Note that modulation is significant for every resonance, as expected from graphenes broadband absorption.

cavity) changes the cavity lineshape from an undercoupled low-Q resonance at 0 V to a progressively more critically-coupled, higher-Q resonance. While the spectrum moves primarily vertically from changes in loss, shifts on the wavelength axis can be attributed to the non-monotonic gate-dependent imaginary conductivity of graphene and are similar to voltage-dependent cavity shifts for graphene integrated on photonic crystal cavities [97–99]. Modulation occurs in every resonance in the 100 nm tuning range of our laser (Figure 3.10). We simultaneously fit all six datasets, allowing each curve to have an independent a and $n_g L$, while forcing t and P_{in} to be shared among all curves. We note that the thus-extracted round-trip transmission (Figure 3.9b) does not saturate at the voltages we measure, indicating that the graphene does not fully enter the Pauli blocking regime. However, because of the inverting nature of the interference effect, even somewhat high residual losses are sufficient for resonator extinction ratios exceeding 28 dB.

3.3.2 Small-signal RF Measurements

The device exhibits a small-signal RF bandwidth of 30 GHz (Figure 3.9c), currently RC limited by the size of the capacitor, graphene sheet resistance, and graphene/metal contact resistance. We measure the transmission modulation with an electrical vector network analyzer and a 45 GHz photodiode by first tuning the laser to the center of the unbiased 1555 nm resonance, then increasing bias to -30 V. The photon lifetime in the ring resonator (~ 160 GHz for $Q=1200$) does not limit the device bandwidth. For conservative estimates of the geometric capacitance (55 fF), roughly half of the ($\sim 100 \Omega$) resistance in the RC circuit comes from the 50Ω transmission line itself. Thus, the intrinsic RC time constant, if driven, for example, by an on-chip source, is likely near 60 GHz. The remaining resistance is a combination of sheet resistance in the ungated graphene ($\sim 500 \Omega/\square$) and contact resistance ($\sim 500 \Omega \cdot \mu\text{m}$), which we estimate via transfer length measurements (TLM) on the same growth of graphene. An equivalent circuit diagram is shown in figure 3.11. With current state-of-the-art contacts of $\sim 100 \Omega \cdot \mu\text{m}$ [85, 95], the intrinsic speed of our device would approach 150 GHz.

3.3.3 Large-signal RF Measurements and Eye Diagrams

To confirm the optical response of our modulator, we measure the large-signal response of the device and observe an open 22 Gbps non-return-to-zero eye diagram (Figure 3.9d). The incoming signal is a 2^7-1 pseudo-random binary sequence (PRBS) at 7.5 V peak to peak without preemphasis and with a -30 V DC bias. To remove reflections caused by the strongly capacitive load of the modulator, we place, adjacent to the incoming signal probe, a second probe with a DC-block

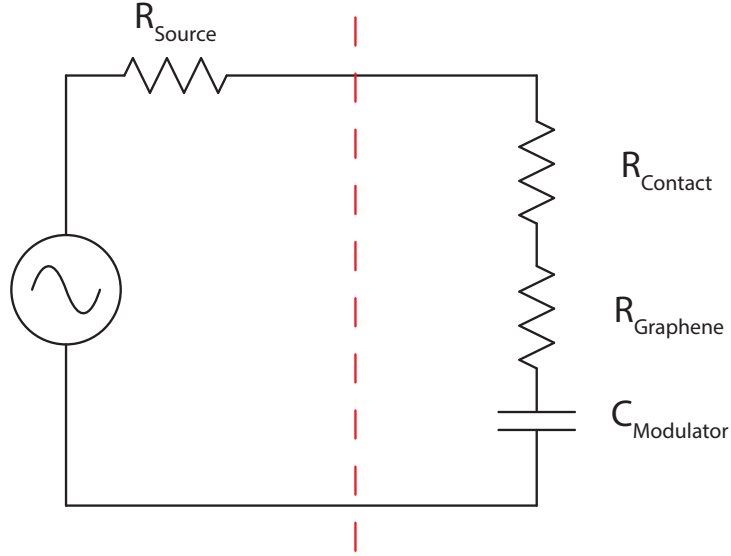


Figure 3.11: Equivalent circuit of driven graphene modulators. The intrinsic device (right of the red dashed line) is a simple RC series circuit, with resistance contributions both from graphene sheet resistance and metal/graphene contact resistance. In experiment, there is an additional resistance R_{source} from the $50\ \Omega$ coaxial line impedance that limits performance to less than the intrinsic RC speed.

capacitor and $50\ \Omega$ RF termination (Figure 3.12). The bandwidth of our eye diagram is primarily limited by cabling losses and the 20 GHz bandwidth of the oscilloscope optical sampling module. Under this configuration, our modulator has a power consumption ($CV^2/4$) of approximately 800 fJ/bit, most of which is dropped on the termination resistor. We note that the DC leakage current is below the measurement floor of the sourcemeter at all voltages, indicating negligible static power consumption. Further, the low thermo-optic coefficient of silicon nitride, together with the relatively low Q of our devices, makes the modulator insensitive to thermal effects.

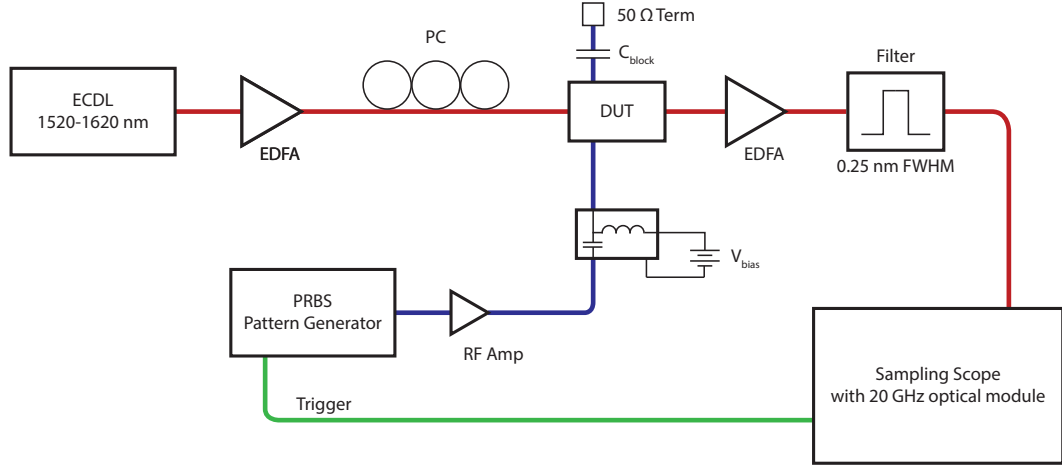


Figure 3.12: Eye Diagram Test Setup. The testing setup consists of an optical (red) and electrical (blue) arm. An external-cavity diode laser is amplified both before and after the chip to compensate for chip facet and fiber component insertion losses, then sent through a bandpass grating filter to remove amplified spontaneous emission noise. RF PRBS signals (Centellax TG1P4A) are amplified in a 40 Gbps modulator driver (Centellax OA4MVM3) and biased before contacting the device with a GGB 40A picoprobe. A second probe blocks DC bias and terminates the RF signal to avoid reflections from the device. Without this second probe, eye diagrams have significant ringing on rising and falling edges from periodic reflections in the feed coaxial cable.

3.3.4 Conclusion

We have demonstrated the first ultrafast graphene modulator by leveraging critical coupling effects on a silicon nitride ring resonator. A key figure of merit for modulators is the bandwidth f_{max} and the modulation depth D_{dB} , relative to the swing voltage V_{swing} and the insertion loss IL_{dB} :

$$FOM = \frac{f_{max} D_{dB}}{V_{swing} IL_{dB}} \quad (3.1)$$

Our modulator achieves a figure of merit of $3.75 \text{ GHz}\cdot\text{V}^{-1}$, compared to $0.16 \text{ GHz}\cdot\text{V}^{-1}$ in low-insertion-loss graphene-on-silicon structures [73] and $0.27 \text{ GHz}\cdot\text{V}^{-1}$

in double-layer graphene electroabsorption devices [71]. Such a dramatic improvement in the figure of merit promises graphene's continued potential as an electro-optic material. Furthermore, the integration of a high-speed and broadband modulator with otherwise completely passive and broadly transparent waveguide materials opens many possibilities in nonlinear optics, quantum optics, and visible photonics.

CHAPTER 4
GRAPHENE LINEAR AND PHASE MODULATION

4.1 Linear Modulation

4.1.1 Device Concept

Carrying analog radio frequency signals over an optical carrier has proven an important application of fiber optic links. Such systems find use in antenna remoting, true time delays for phased array radar, and large-array radio astronomy, among others [19]. These applications, however, place more stringent requirements on modulators than do digital communications, as analog modulation must be low-noise and distortion-free (that is, highly linear) while not sacrificing insertion loss or extinction ratio.

Despite their promise for low-cost integrated optics, silicon plasma-dispersion effect modulators are fundamentally nonlinear because of the square root carrier depletion behavior of the PN diode (Figure 4.1a) [100]. While many researchers have attempted to improve the linearity of silicon modulators, these techniques often rely on resonance [101, 102] or require careful phase matching [103] that reduce their optical bandwidth or add complexity. Electroabsorption modulators based on III-V structures can be extremely linear [104], but they require careful control of input optical power and bias voltage. Further, both these and traditional lithium niobate linear modulators [105] are not easily integrated with CMOS electronics.

Here we demonstrate that graphene-on-silicon nitride modulators, in contrast, are fundamentally linear. In graphene modulators [68, 71], voltage applied to a

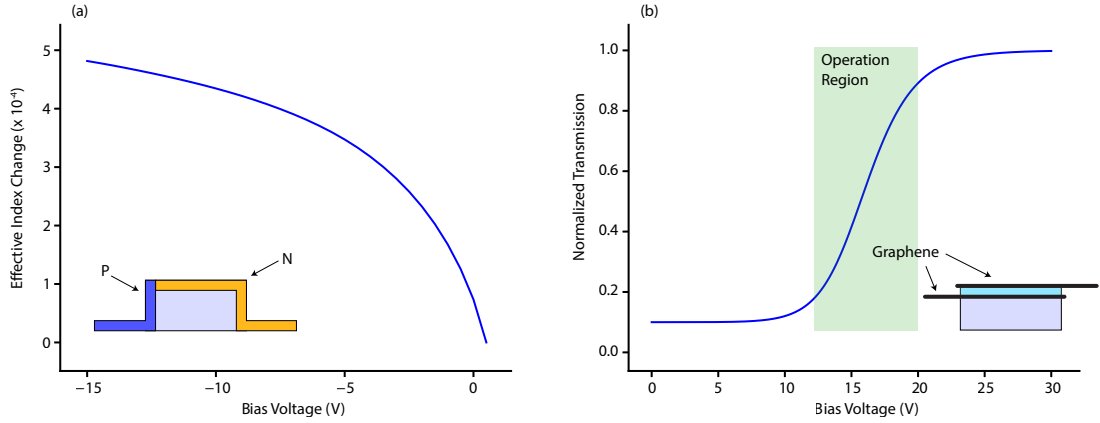


Figure 4.1: Comparison between inherently nonlinear silicon plasma-dispersion modulators and inherently linear graphene modulators. **a.** TCAD simulation of effective index change versus bias voltage for a silicon PN junction modulator. Inset: doping cross-section of the simulated modulator. **b.** Calculated transmission versus bias voltage for a graphene electroabsorption modulator, from equation 4.1. Inset: modulator cross-section showing graphene-insulator-graphene capacitor.

graphene-insulator-graphene capacitor gates the Fermi level of the graphene sheets, changing their absorption through Pauli blocking of the interband electron transitions [77]. The transition from absorbing to transparent is gradual, governed by the Fermi-Dirac distribution of electrons in the bands at room temperature (Figure 4.1b). Graphene’s interband absorption as a function of Fermi level is described by [97]:

$$\alpha = \frac{\alpha_0}{2} \left[\tanh \left(\frac{\hbar\omega + 2|E_F|}{\Gamma} \right) + \tanh \left(\frac{\hbar\omega - 2|E_F|}{\Gamma} \right) \right] \quad (4.1)$$

where E_F is the graphene Fermi level and Γ is the interband transition broadening. Γ is strongly dependent on the scattering rate in the graphene. Thermal scattering sets a limit of $\Gamma \geq 4k_B T$, but even at room temperature the broadening is dominated by defect or impurity scattering in all but the cleanest graphene [106–111]. Encapsulation in hexagonal boron nitride [12, 112], in particular, provides an ex-

ceptionally electronically-clean environment and can show Γ values at or below 100 meV.

Because the graphene modulator is at its core a capacitor, the accumulation of carriers on the graphene is characteristically linear with voltage:

$$E_F = \hbar v_f \sqrt{\pi \left(n_0 + \frac{C|V|}{q} \right)} \quad (4.2)$$

Here C is the capacitance per unit area ($C = \epsilon_0 \epsilon_r / d$) and v_f is the graphene Fermi velocity. Usually $v_f \approx 10^6$ m/s, but recent work [113] has shown tunability between 1×10^6 and 3×10^6 m/s depending on the underlying substrate.

Graphene modulators are especially linear because the large linear region of the sigmoidal Fermi-Dirac distribution transfers those charge modulations to the optical carrier without distortion across a wide range of bias voltages. The devices here are simple straight-waveguide electroabsorption modulators, and use neither the ring coupling enhancement of chapter 3 or explicit linearization techniques.

4.1.2 Modulator Fabrication

We fabricate the modulators with CVD-grown graphene in a multi-layer process very similar to the ring modulator. Waveguides consist of PECVD silicon nitride deposited on a thick thermal oxide layer and patterned with deep-UV lithography. Rather than CMP, we smooth the abrupt steps in the nitride film with PECVD deposition and reflow of borophosphosilicate glass (BPSG). This reflow technique is easier and faster than CMP and does not require additional equipment, but lowers modulator performance because the graphene is farther from the mode center. On

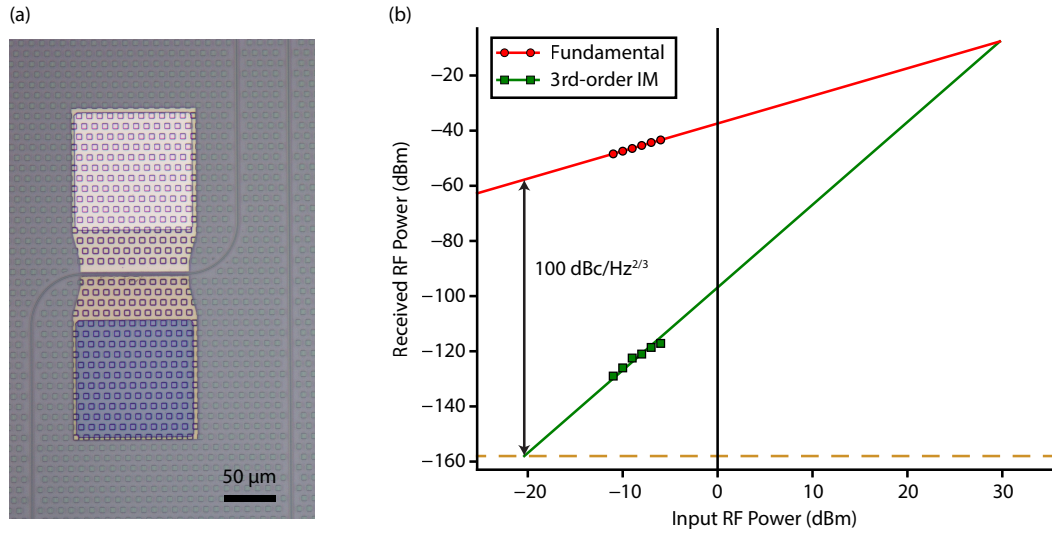


Figure 4.2: Device design and linearity measurements. **a.** Optical microscope image of the fabricated device. The graphene/alumina/graphene capacitor lies between the two contacts along the waveguide. **b.** Two-tone intermodulation response of the modulator centered at 2.5 GHz. Dashed line is the calculated noise floor.

top of this planarizing layer, we transfer and pattern single-layer graphene grown via CVD on copper foil and create Ti/Pd contacts via electron beam evaporation and lift-off. A 65 nm ALD alumina gate dielectric divides this graphene sheet from a second layer of graphene and metal contacts. The device is finally clad with 10 nm ALD alumina and vias are opened down to the contacts to allow electrical probing. Inverse nanotapers for fiber to chip coupling function well without the need for a thick cladding SiO₂ layer. The finished device, with an active length of 100 μm, is shown in Figure 4.2a.

4.1.3 Linearity Measurement and Spurious-free Dynamic Range

We measure the linearity of the modulators with a standard two-tone intermodulation distortion test (Figure 4.3). To do this, we drive the modulator simultaneously with two closely-spaced sine wave carriers (ω_1 and ω_2), collect the output light in a photodiode, and then measure the power of the carriers and their mixing products in an RF spectrum analyzer. Nonlinearity in this system is dominated by the modulator voltage transfer function, which causes a series of harmonics to appear. Second-order (quadratic) distortion creates the second harmonic as well as sum and difference products of the two input frequencies, while third-order distortion, much like optical four-wave mixing, creates a number of intermodulation products, notably $2\omega_1 - \omega_2$ and $2\omega_2 - \omega_1$. Note that all of the second-order harmonics appear at frequencies far away from the drive frequencies. Because almost all useful RF systems have sub-octave bandwidth, these can easily be filtered out, so only third-order distortion remains relevant.

We vary the power of the input signals and observe the change in received power of both the desired fundamental and these mixing products. The fundamental varies linearly with applied power, while the third-order products vary as P_{in}^3 and thus drop much faster with lower applied powers than the fundamental does. We can plot these on a log-log scale (Figure 4.2b) and fit lines with fixed slopes of 1 and 3 to the data, allowing the intercept to be the only fitting parameter since the distortion order is known a priori.

The spurious-free dynamic range (SFDR) is the maximum achievable distance between the fundamental and the highest noise or distortion spur. It is a measure

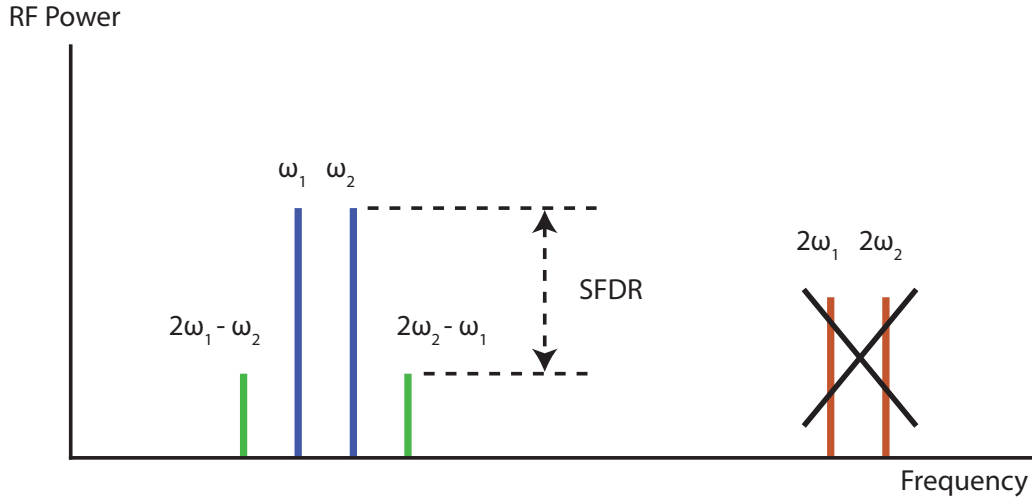


Figure 4.3: A conceptual view of harmonic generation and the definition of SFDR. Nonlinear mixing between two frequencies ω_1 and ω_2 yields both out-of-band second harmonics (red), which can be ignored, and in-band mixing products (green), which limit linearity. SFDR is the largest dynamic range between the carriers and either these mixing products or the noise floor.

of the ultimate lowest distortion the modulator can produce, with units $\text{dBc}/\text{Hz}^{2/3}$. The $\text{Hz}^{2/3}$ factor exists because the noise power varies with bandwidth; a larger bandwidth causes the maximum dynamic range to lie at a higher input power, further up the distortion line. dBc is used here because SFDR is dB relative to the fundamental carrier. A similar metric is IIP_3 , the third-order input intercept power, that is, the input power at which the fundamental and third-order intermodulation lines intersect. OIP_3 is sometimes also specified; it is the output power at this same point and is simply the sum of IIP_3 and the end-to-end system RF loss: $\text{OIP}_3 = \text{IIP}_3 + \text{IL}$.

With this modulator we measure a spurious-free dynamic range of $100 \text{ dBc}/\text{Hz}^{2/3}$ and an input third-order intercept point of 30 dBm at 2.5 GHz (Figure 4.2b). We drive with two sine wave carriers spaced 100 MHz apart, at 2.45 and 2.55 GHz , measuring their mixing product ($2f_2 - f_1$) at 2.65 GHz . Notably, both

SFDR and modulation depth remain relatively constant over a wide range of bias voltages. The modulator receives 30 mW optical power in the waveguide at 1550 nm, and an EDFA is added after the chip to compensate for approximately 10 dB modulator insertion loss and 15 dB fiber-to-chip coupling loss, boosting the optical power at the photodetector to 15 mW, for 10 mA of DC photocurrent. With this link, an applied RF power of -5 dBm (356 mVpp) causes a received RF power of -42 dBm. We calculate a noise floor of -158 dBm/Hz by assuming a shot noise limited 100 mW laser source with negligible fiber-to-chip coupling losses and adding noise figure contributions from modulator insertion loss, EDFA, and detector responsivity [114]. Notably, because the EDFA is a quantum amplifier operating on photons that obey Poisson statistics, even a theoretically perfect optical amplifier has a noise figure of 3 dB.

4.1.4 Theoretical Model

To simulate the linearity of the graphene modulator, we can take a Taylor expansion of equation 4.1, combined with equation 4.2, at various voltage bias points. With $\epsilon_r = 9.8$, $d = 60$ nm, and $v_f = 10^6$ m/s, this yields the values in Figure 4.4. Note that the second-order term is minimized at the center, where the transmission function (Figure 4.1b) appears most linear. The third-order term responsible for the intermodulation distortion, on the other hand, becomes minimized at the shoulder of the function where the third derivative goes to zero. SFDR is roughly proportional to the ratio of the first-order to the third-order Taylor coefficient. While operating at the peak of the first-order curve (highest extinction ratio point) gives acceptable linearity, performance can be improved even further by carefully

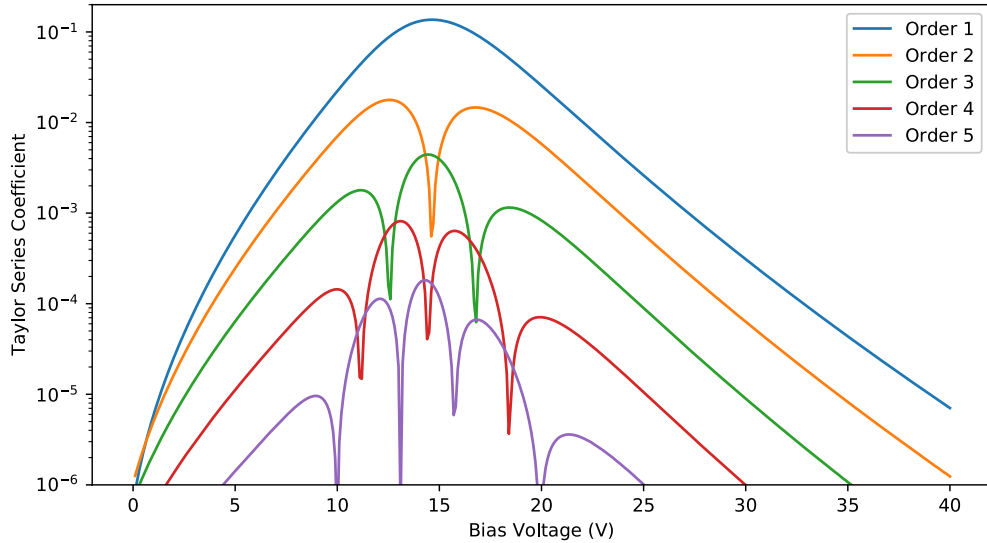


Figure 4.4: Taylor coefficients of the graphene modulator transfer function about a range of bias voltages. Notice that there are several voltages for which higher-order terms vanish while the first-order term remains high, which would effectively eliminate those harmonics.

biasing into these corners where the third-order term drops away. This gives rise to the SFDR peaks in Figure 4.5.

Using this careful voltage control, the SFDR can be extended to over 120 dBc/Hz^{2/3}. Increasing device length or graphene overlap with the optical mode can also drastically increase slope efficiency and thus link gain and SFDR. Intuitively, since SFDR is limited by noise, achieving a modulator signal farther above the noise floor will improve SFDR as well. Additionally, the robustness of graphene modulators allows large optical power handling, decreasing noise figure when paired with detectors with high saturation current. Because of graphene's unprecedented mobility, such modulators could extend on-chip linear modulation towards 100 GHz, unlocking millimeter wave radio over fiber links.

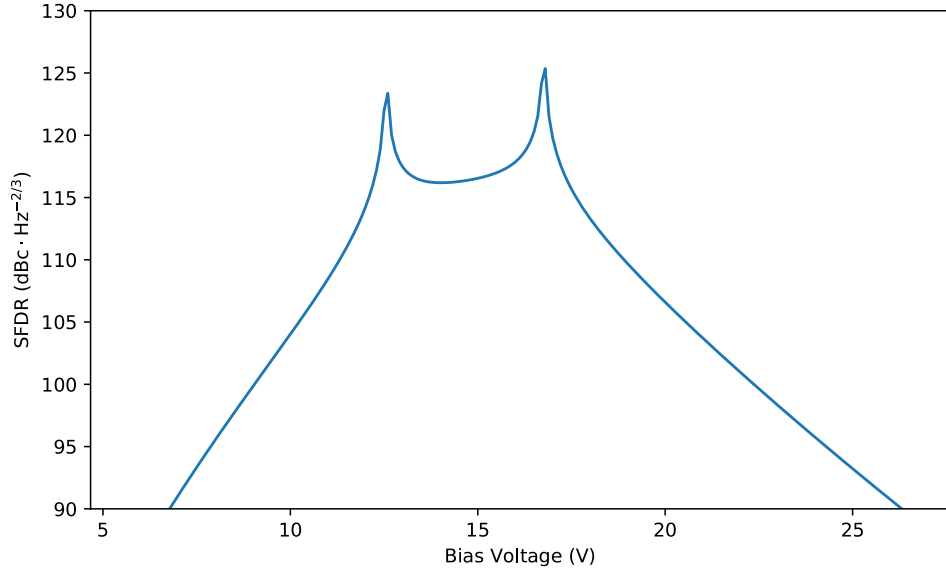


Figure 4.5: Simulated spurious-free dynamic range of the graphene electroabsorption modulator over a range of bias voltages. $115 \text{ dBc/Hz}^{2/3}$ is achievable over a wide voltage, with $>120 \text{ dBc/Hz}^{2/3}$ possible near the peaks of the curve where the 3rd-order coefficient is minimized.

4.2 Binary Phase Modulation

While high-speed graphene modulators discussed so far seem to have a bright future, they notably only modulate the optical amplitude, not its phase. For advanced communication systems, particularly those in long-haul telecommunications, we generally prefer phase modulation, where the amplitude of the light stays constant but data is encoded in rapid switching of the phase of the optical carrier. Indeed, in most photonics modulators are natively phase (or refractive index) switching devices, which need to be converted into amplitude modulators via interferometers or resonators. Graphene, however, changes index only weakly with changes in applied voltage. While pure graphene refractive index modulators appear possible [115–117], they require bias voltages near or exceeding the breakdown field of the dielectric, making fabrication challenging and long-term

reliability uncertain. Can we instead, analogously to the interferometer, build a phase modulator out of pure absorption modulation? Indeed, we show here that pure binary phase modulation can be created from pure loss modulation by changing the round-trip loss of a ring resonator with a carefully engineered coupling coefficient.

Recall the electric field transmission of a ring resonator (equation 2.6 on page 13):

$$\frac{E_2}{E_1} = \frac{t - ae^{i\phi}}{1 - ate^{i\phi}}$$

While before we only dealt with the power transmission $|E|^2$, the ring resonator also modifies the phase of the transmitted light, as shown in Figure 4.6. Far away from resonance the phase is basically unperturbed, but on-resonance the bus waveguide phase depends strongly on the round-trip loss and phase of the ring. In particular, there is a π jump in phase between undercoupled and overcoupled resonances for light perfectly on-resonance.

Now that we have opened the possibility of phase modulation, the key figure of merit is not the extinction ratio in power, but rather the distance between modulation points in the complex (I-Q) plane. By plotting the real part of the light on the x-axis and the imaginary part on the y-axis, we can visualize modulation of both amplitude (radial distance from the origin) and phase (angle about the origin) simultaneously. To find this optimum, we solve for the complex distance between two points, one with $a = 0.5$ and one with $a = 0.7$, corresponding to experimentally-achievable round-trip losses from our amplitude modulator experiment (Figure 3.9b). Plotting this distance versus both t and ϕ gives Figure 4.7.

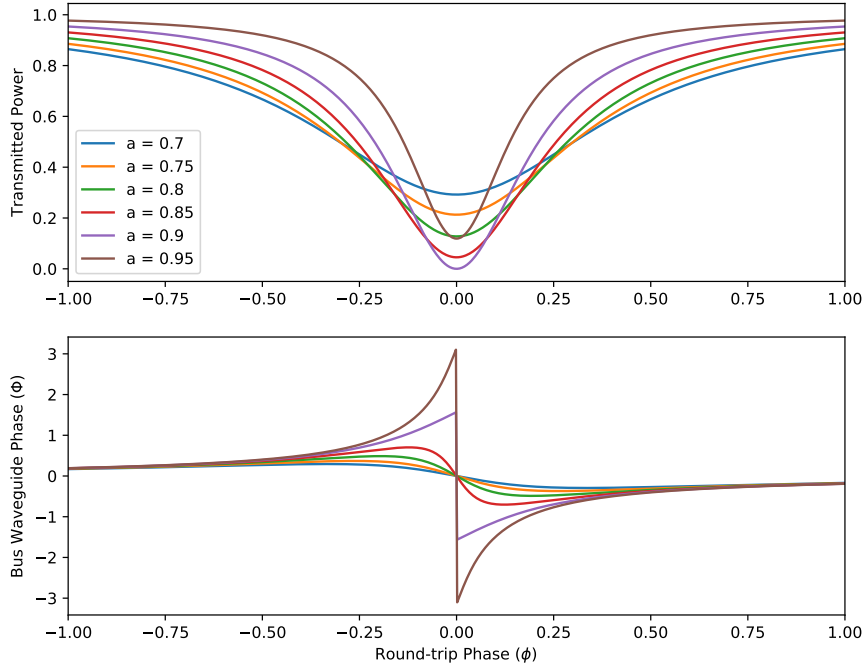


Figure 4.6: Bus-waveguide power ($|E_2/E_1|^2$) and phase response ($\arg(E_2/E_1)$) of a ring resonator with coupling strength $t = 0.9$ and various values of round-trip loss a .

For comparison, amplitude modulation for the same conditions is plotted in Figure 4.8.

Note that the maxima for both of these contour plots occur directly on-resonance ($\phi = 0$). The optimum coupling strength is different for complex and amplitude modulation, however, at $t = 0.61$ and $t = 0.7$ respectively. For complex modulation, we want critical coupling to be roughly evenly between the achievable round-trip losses, while for amplitude modulation we place critical coupling at one of the endpoints. The position of the optimum for complex modulation hints at the underlying mechanism: the ring is switching from undercoupled to overcoupled and thus accumulating the associated π phase shift.

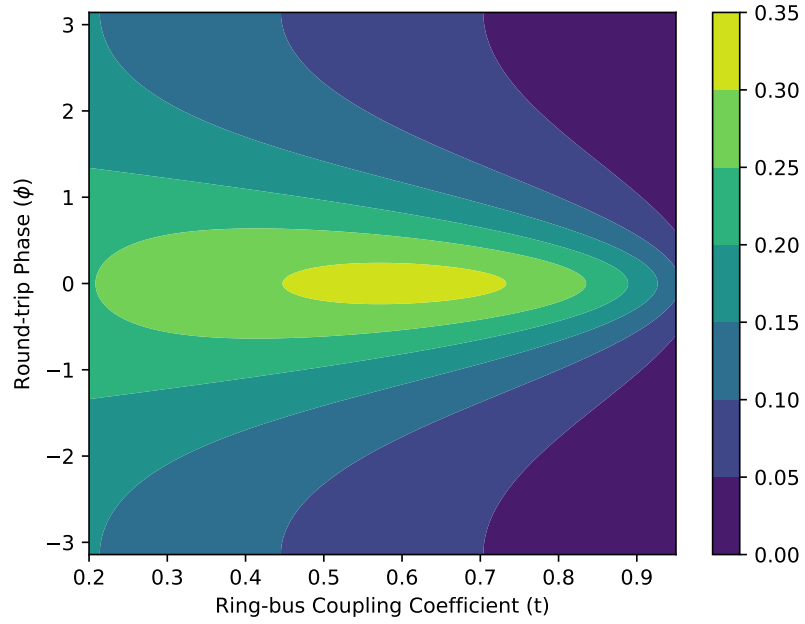


Figure 4.7: Contour plot of complex modulation amplitude (I-Q plane distance, $|E(a_1) - E(a_2)|$) versus ring round-trip transmission and phase. Round-trip loss a varies between 0.7 and 0.5, and round-trip phase $\phi = 0$.

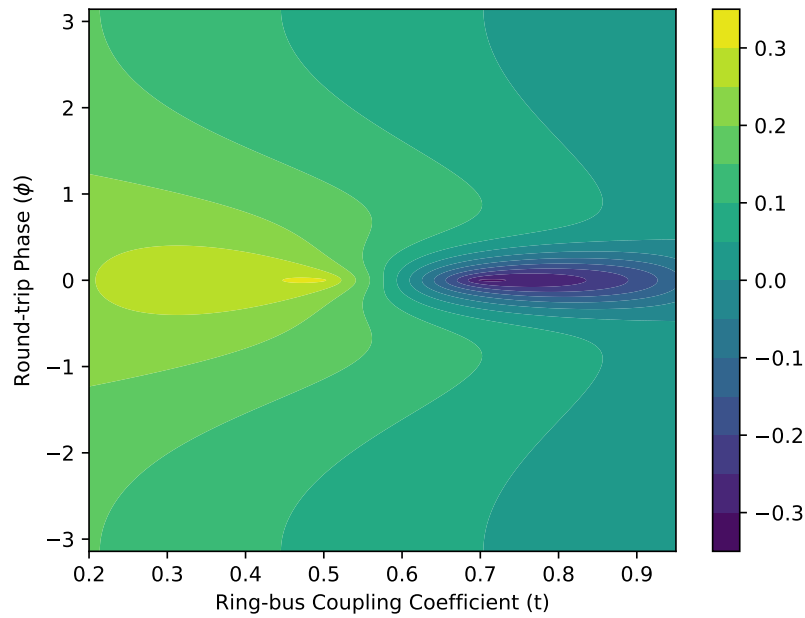


Figure 4.8: Contour plot of power-only modulation amplitude ($|E(a_1)| - |E(a_2)|$) versus ring round-trip transmission and phase. Round-trip loss a varies between 0.7 and 0.5, and round-trip phase $\phi = 0$.

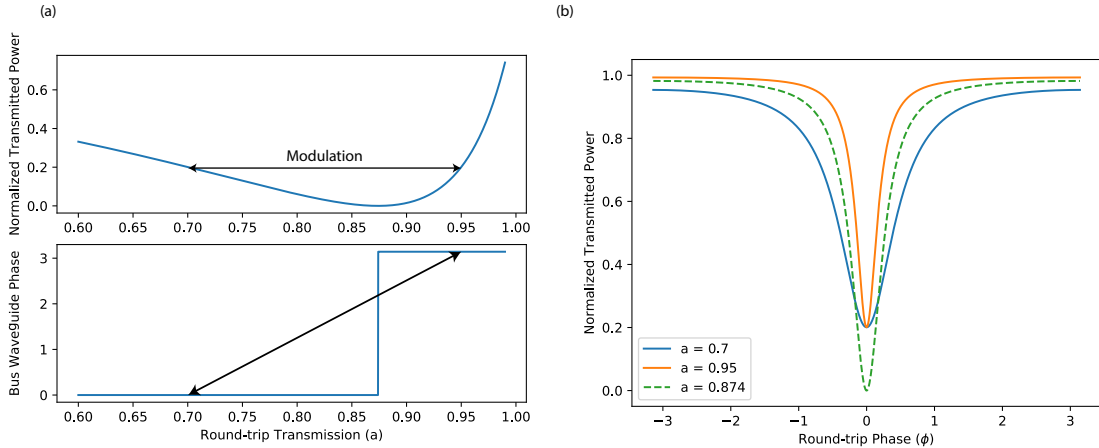


Figure 4.9: Binary phase modulation without amplitude change. **a.** Ring resonator bus waveguide transmission (top) and phase (bottom) on resonance for coupling coefficient $t = 0.874$ and varied round-trip transmission a . Note the abrupt π phase change passing through critical coupling, and how a pair of a values (0.7 and 0.95) have the same transmission but are out of phase. **b.** Spectra of matching undercoupled and overcoupled resonances, and a critically-coupled resonance for comparison. All share $t = 0.874$.

Figure 4.9a, a cut through this curve for $\phi = 0$, demonstrates this instantaneous phase modulation. It is possible to pick two a points on this curve which give the same transmitted power but opposite phases, thus creating digital binary phase-shift keying (BPSK). While full analog control over the phases is not possible, such control is unnecessary or even unwanted for BPSK. Changing the exact a values simply changes the output power, not the phase. For two a that have the same output power, we get pure phase modulation, corresponding to an undercoupled and overcoupled resonance with the same extinction ratio (Figure 4.9b). The extinction ratio of this resonance becomes the insertion loss of the phase modulator; lower round-trip loss enables higher optimum t and less insertion loss. Insertion loss is less critical in phase modulation systems because they typically use heterodyne detection to amplify the small received signal over the detector noise floor and achieve shot noise-limited signal to noise ratio.

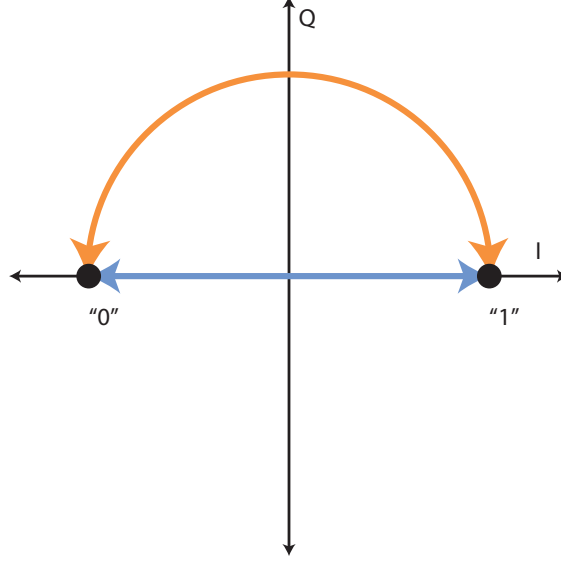


Figure 4.10: I-Q diagram of binary phase shift keying. Blue arrows indicate the path of the graphene ring BPSK modulators between the 1 and 0 constellation points. Orange arrows indicate the path of a traditional phase modulator.

In the I-Q plane, we can visualize this modulation as switching between two points on the I-axis via a path through the origin (Figure 4.10). This behavior contrasts with traditional phase modulator BPSK, where the path is along a constant-radius circle. Other than dips in signal power during the switching, however, the behavior is identical.

Going forward, implementing this modulator in a graphene-clad ring requires strong and precise coupling so we can fully reach an overcoupled resonance even with residual (un-gateable) graphene loss. Improving graphene material quality is key to achieving full gating. One might also consider variable ring to waveguide coupling control [118, 119] to precisely balance the undercoupled and overcoupled resonances. Doing so can open up chip-scale phase modulation at unprecedented speeds.

HALF-WAVELENGTH PITCH OPTICAL PHASED ARRAY**5.1 Device Concept**

Chip-scale optical phased arrays [120–134] enable ultracompact beam steering and LIDAR for autonomous vehicles, precision robotics, and free-space optical communications. Because these applications demand very wide angle beam steering with very high emitted beam quality, a natural choice is to place array emitters at a half-wavelength pitch, as is common in radiofrequency phased arrays. In optics, however, such tight pitches are nearly impossible because the optical mode size itself is close to a wavelength, and so arrays must use a coarser pitch and sacrifice field of view and efficiency. Here we overcome these limitations with an anti-crosstalk design that enables tightly-packed emitters, demonstrating the first scalable optical phased array with half-wavelength pitch. Our array emits a single diffraction-limited beam over a full 180 degree field of view, even when steered up to 60 degrees off-axis. The 63% beam forming efficiency promises to enable photon-starved LIDAR ranging.

Optical phased arrays to date, despite ever-increasing array size and element count [125, 132], remain strongly limited in beam quality and maximum steering angle because unwanted coupling between dielectric waveguides forces emitters to be placed several microns apart. Emitter spacing greater than half a wavelength steals optical power from the main beam [135], redirecting it into unwanted periodic grating lobes tens of degrees away that limit the uniquely addressable steering range of the array. While strong confinement in metals makes half-wavelength spacing possible in RF arrays, the nearby plasmon resonance makes such ap-

proaches [136, 137] impractically lossy at optical frequencies. One group [131] has achieved half-wavelength emitter pitch in dielectric waveguides by minimizing the length over which they run close together, but that approach shows poor beam quality and does not scale to large numbers of waveguides. Creative solutions to achieve wide field of view, like non-uniform emitter pitch [123, 125, 138], successfully suppress grating lobes but redirect the power carried in them randomly rather than back into the main beam. Power thus redirected is effectively lost, severely degrading received signal power for LIDAR. For the typical emitter pitches of 2-3 μm required to avoid coupling over millimeter-scale propagation lengths, fill factor remains below 20 percent, and power in the main beam, even theoretically, rarely exceeds 30-40 percent of the total array output.

We simultaneously achieve wide steering angle and high beam efficiency by designing an end-fire optical phased array at true half-wavelength pitch, engineered to avoid coupling between closely-spaced output waveguides even over millimeter-scale propagation lengths. In order to minimize coupling, we exploit the fact that arrays of waveguides that are mismatched in phase velocity couple weakly even if their evanescent fields overlap [139], since maximum power coupling between two waveguides varies as $1/((\Delta\beta/2\kappa)^2 + 1)$, where $\Delta\beta$ is the difference in propagation constant and κ is the field overlap coupling strength. We choose the widths of the output waveguides to have high dispersion ($\partial\beta/\partial w$), so that phase mismatch can be achieved with only small changes in the waveguide width. Roughly equal widths ensure uniform illumination of the phased array aperture since the powers in all waveguides are equal. In our design waveguides are phase-mismatched with both their nearest neighbor and with their second-nearest neighbor by cycling through a set of three widths (300, 350, and 400 nm, in sequence; Figure 5.1a). The 250 nm waveguide height ensures all of these waveguides are single-mode for TE polarized

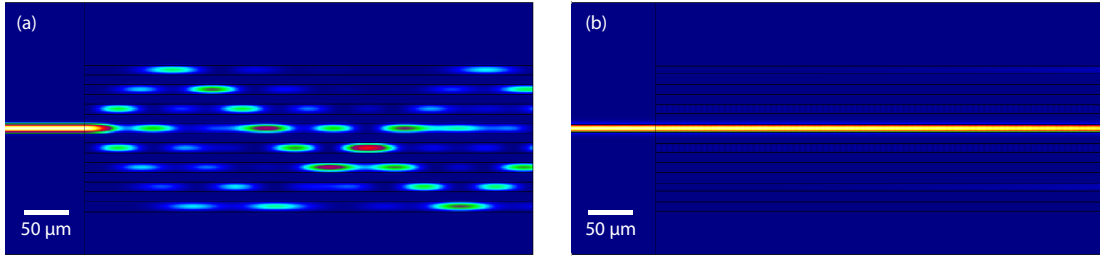


Figure 5.1: Waveguide array avoided coupling. **a.** Eigenmode expansion simulation of an array of waveguides with equal width of 400 nm on 775 nm pitch. Light is launched into a single waveguide from the left and couples strongly when adjacent waveguides are introduced. **b.** Simulation of the waveguide array with sequentially varying widths of 300, 350, and 400 nm. Light is launched into the 300 nm wide waveguide, and less than 3% coupling is observed, only to the waveguides with equal width.

light. We find that for the < 0.5 mm propagation lengths in this experiment, coupling between third-nearest neighbors (waveguides with equal width separated by 1.5λ) is negligible and power propagates only in the waveguide it was launched into (Figure 5.1b).

5.2 Beam Steering Experiment

5.2.1 Device Design and Fabrication

We demonstrate wide-angle beam steering with a 64-channel thermooptically-steered silicon phased array. A tree of cascaded 1x2 MMI splitters divides a 1550 nm input laser into 64 separate outputs, each of which is followed with an individual phase shifter (Figure 5.2b). Phase shifters are initially placed on a $20 \mu\text{m}$ pitch to minimize thermal crosstalk; after the phase shifters we route the waveguides in a nested 90° bend to form the final 775 nm pitch (Figure 5.2c). The $200 \mu\text{m}$

bend radius is sufficiently large to not significantly perturb the effective index of the waveguides and thus minimizes coupling as they are brought close together. The dense array of waveguides exits the edge of the chip through a low-roughness plasma-etched facet [34]. Each phase shifter consists of a thin platinum wire separated from the waveguide by 1 μm of top cladding oxide. Thick aluminum wires then route each microheater to a bond pad at the chip perimeter and tie the opposite ends of the heaters together in a low-resistance common ground. We mount the chip with high thermal-conductivity silver sintering paste directly to an aluminum heatsink and wirebond each heater to an attached printed circuit board (Figure 5.2d). A 64-output digital-to-analog converter (NI PXIe-6739) drives each microheater individually, allowing arbitrary phase control over more than 2π .

5.2.2 Far-field Measurement

We experimentally achieve grating-lobe-free operation over an entire 180° field of view with the beam steered up to $\pm 60^\circ$ off-axis (Figure 5.3a). We place a single-element, 1 mm diameter photodiode in the Fraunhofer far-field approximately 20 cm away from the chip and use a phase-aware optimization algorithm to align the initially random output phases and converge a beam centered on the fixed detector position. To measure emission patterns over such a large field of view, we design a mechanically-scanned far-field imager by rotating that same photodiode on an optical rail about the chip output facet, in-plane with the waveguides, collecting power as a function of output angle. Compared to typical microscope-like far-field imaging setups, this system has both infinite field of view (rather than the approximately 80° typically imposed by objective numerical aperture) and also lacks aberrations that would limit beam quality. We additionally mount a large cylin-

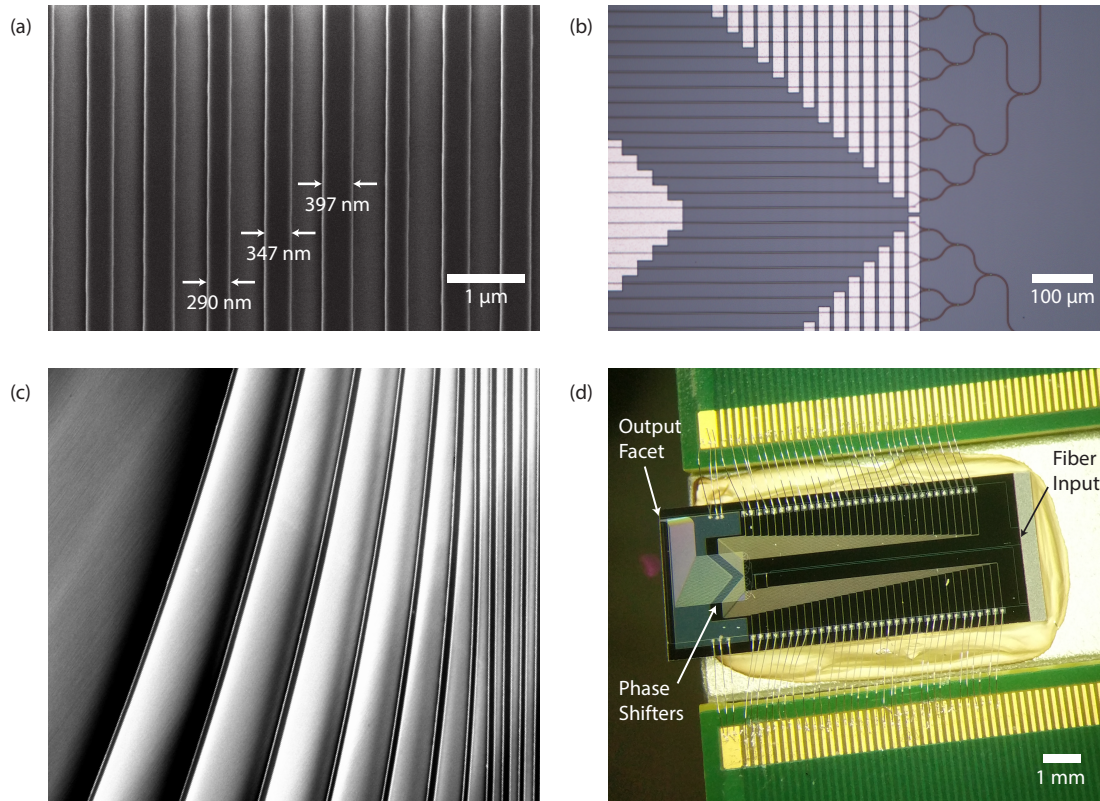


Figure 5.2: Fabricated device. **a.** Top-view scanning electron micrograph of the varying waveguide widths on equal 775 nm pitch. **b.** Optical micrograph of part of the splitter tree, thermo-optic phase shifters, and aluminum wires. **c** Top-view scanning electron micrograph of the nested 90° bend that converts between coarse pitch phase shifters and fine-pitch output waveguides. **d.** Stereoscope image of the wire-bonded chip on its heatsink. Over 90% of the chip area is dedicated to fan-out wiring to match the 200 μm trace pitch on the PCB. Note the output facet overhangs the heatsink to ensure an unobstructed 180° view of the output beam.

drical lens on the rotating arm to focus the vertical fan of emitted light onto the detector for improved signal to noise ratio. Doing so does not affect the behavior of the phased array because the lens has no curvature in the phase-tuned axis. To maximize signal to noise ratio and discard stray light from the fiber-to-chip coupling, we modulate the output light at 1 kHz with an on-chip thermal Mach-Zehnder modulator placed before the splitter tree and use lock-in detection on the far-field photodiode. Beams pointing in other directions can be re-optimized with

the detector moved to the desired angle. Total phase shifter power consumption regardless of beam position is approximately 600 mW, with each phase shifter consuming on average P_π .

5.2.3 Analysis and Discussion

Our array shows output beam quality close to the theoretical maximum (Figure 5.3b). We achieve an 11.4 dB peak to sidelobe ratio over the entire 180° field of view for a beam emitted normal to the array, to our knowledge the best demonstrated to date. The theoretical limit is 13 dB, from the sinc^2 diffraction pattern of a uniformly-illuminated rectangular aperture. Beam width (FWHM) is a diffraction-limited 1.2° , corresponding to the $49.6 \mu\text{m}$ wide aperture. Even when steered 60° off-axis, the peak to sidelobe ratio of our array drops to only 7.2 dB, caused simply by the drop in main beam power because of the \cos^2 dipole-like single-emitter envelope. At such sharp steering angles the beam broadens to 2.3° because the glancing angle decreases the apparent size of the aperture. Beam quality both on- and off-axis is likely limited only by uncontrolled phase in 2 of the 64 emitters due to microheater yield and by phase uncertainty in each channel caused by detector noise in the beam convergence process.

63 percent of the power in the forward-steered beam is concentrated in the main lobe, at least twice that expected in randomized coarse-pitch arrays. In-beam power, as shown in Figure 5.3c, is the cumulative integral in both directions from the beam center, divided by the integral over the entire 180° measurement. Theoretically, our tightly-packed waveguide approach directs 90% of the total output power into the main beam (the integral of a sinc^2 function between the first nulls). Power outside the main beam causes multiple problems in LIDAR systems.

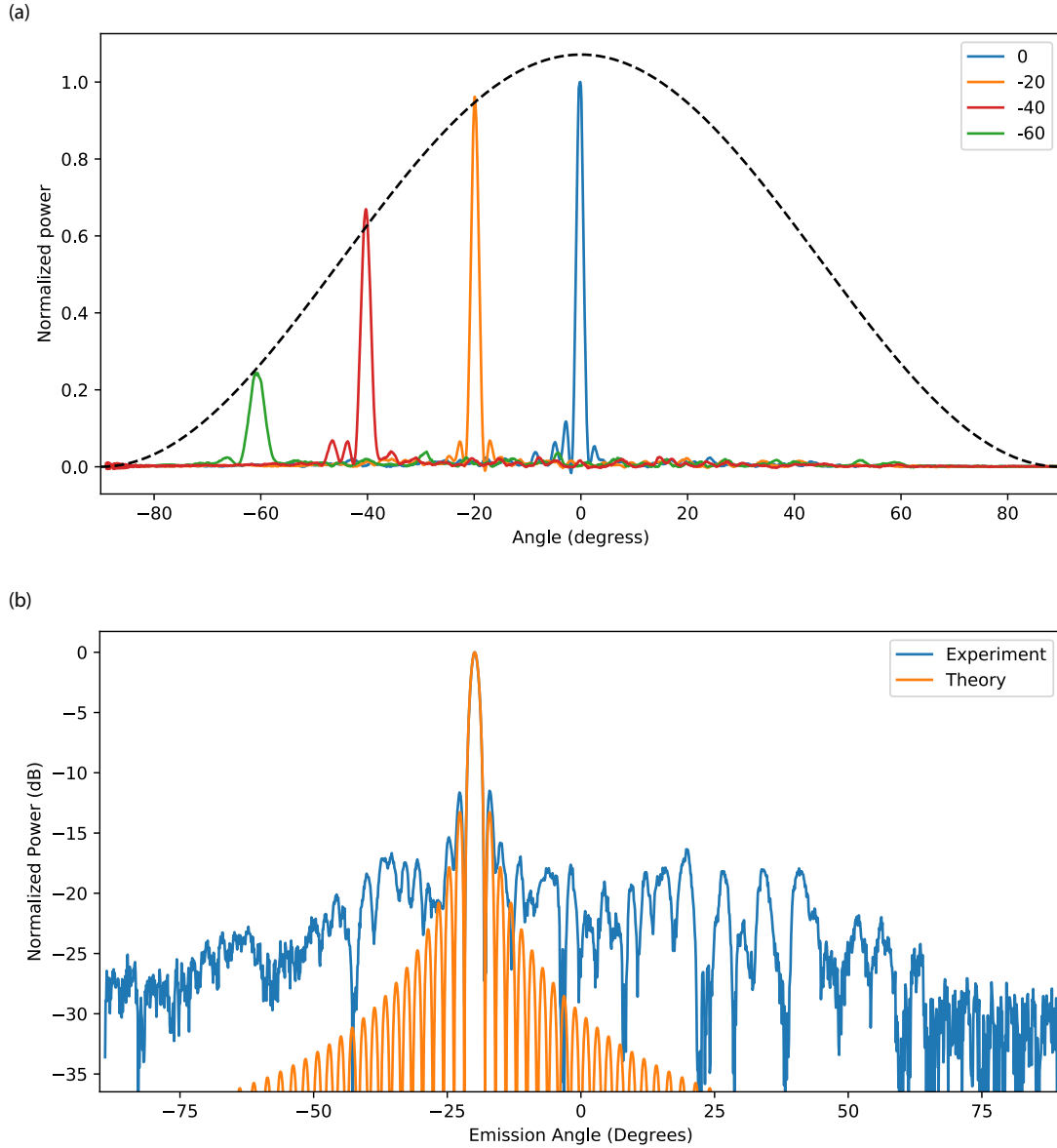


Figure 5.3: (a) Far-field optical power versus output angle over a 180° field of view for several different target beam angles. Power is normalized to the 0° peak but relative amplitudes are as-measured, caused by the \cos^2 dipole-like emitter envelope (dashed line). (b) Logarithmic scale plot of beam steered to -20° and sinc^2 fit.

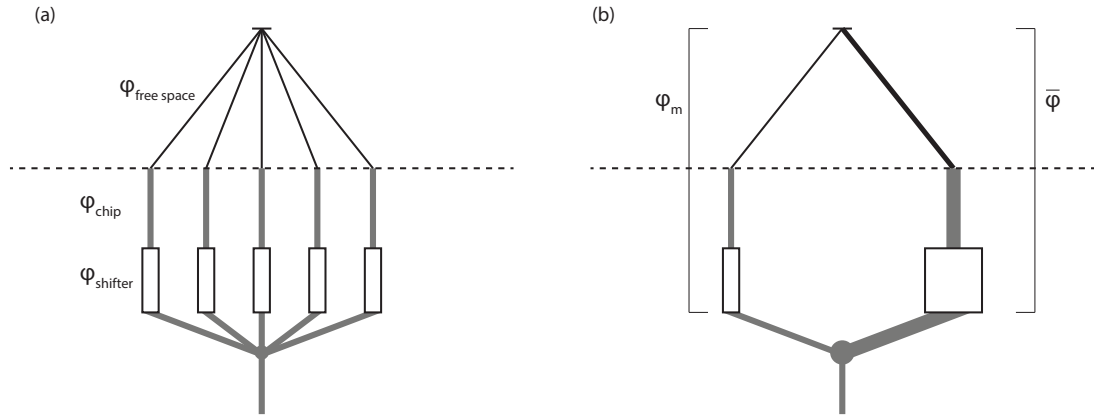


Figure 5.4: Model phased arrays. **a.** Phased array with each contribution to ϕ_n at detector. **b.** Phased array as unbalanced Mach-Zehnder interferometer.

Most directly, this off-axis power is lost from the desired beam twice, in both transmit and receive directions. Additionally, the power hits and returns from other objects, creating false images or, even if no one reflection is strong, raising the overall background of returned signal and obscuring far-away or low-reflectivity targets. The densely-filled arrays demonstrated here are the only known method for avoiding these effects through high-quality beamforming.

We have demonstrated an all-dielectric optical phased array with true half-wavelength emitter pitch that generates nearly diffraction-limited output beams over a full 180° field of view. Our anti-crosstalk design maintains beam quality even at very small emitter spacing, allowing high fill factors, and scales well to a large number of channels. Such systems will enable the next generation of extremely small and light long-range LIDAR.

5.3 Phased array beam convergence algorithm

To converge the initially random phases of each output channel we develop a sequential algorithm that optimizes each channel one at a time against the mean phase of the array. Consider the model N-channel phased array in Figure 5.4. After exiting the 1:N splitter, each channel acquires a phase offset from multiple contributions: $\phi_{shifter}$ from the deliberate controllable phase shifter, ϕ_{chip} from propagation length between the splitter and the output facet, and $\phi_{freespace}$ from the distance between the output facet and the target or detector. We then represent the total phase of the light from channel n at the detector as $\phi_n = \phi_{shifter} + \phi_{chip} + \phi_{freespace}$. In the far-field in broadside (0°) operation, all the lengths ($\phi_{freespace}$) from each channel to the detector are equal, so forming a beam at the detector is equivalent to lining up the phases at the output facet of the chip. Similarly, moving the detector left or right in the far field lengthens some $\phi_{freespace}$ with respect to others, requiring a phase tilt at the facet for constructive interference at the detector. Bringing the detector closer, into the Fresnel region, makes the outer channels travel noticeably farther than the inner channels, so constructive interference requires a phase curvature at the chip facet and therefore a focusing beam. In all cases, the beams from each channel coherently sum:

$$E_{det} = \sum_n a_n e^{i\phi_n} \quad (5.1)$$

where a_n is the amplitude of channel n , and our goal is to choose the set of ϕ_n such that $|E_{det}|^2$ is maximized.

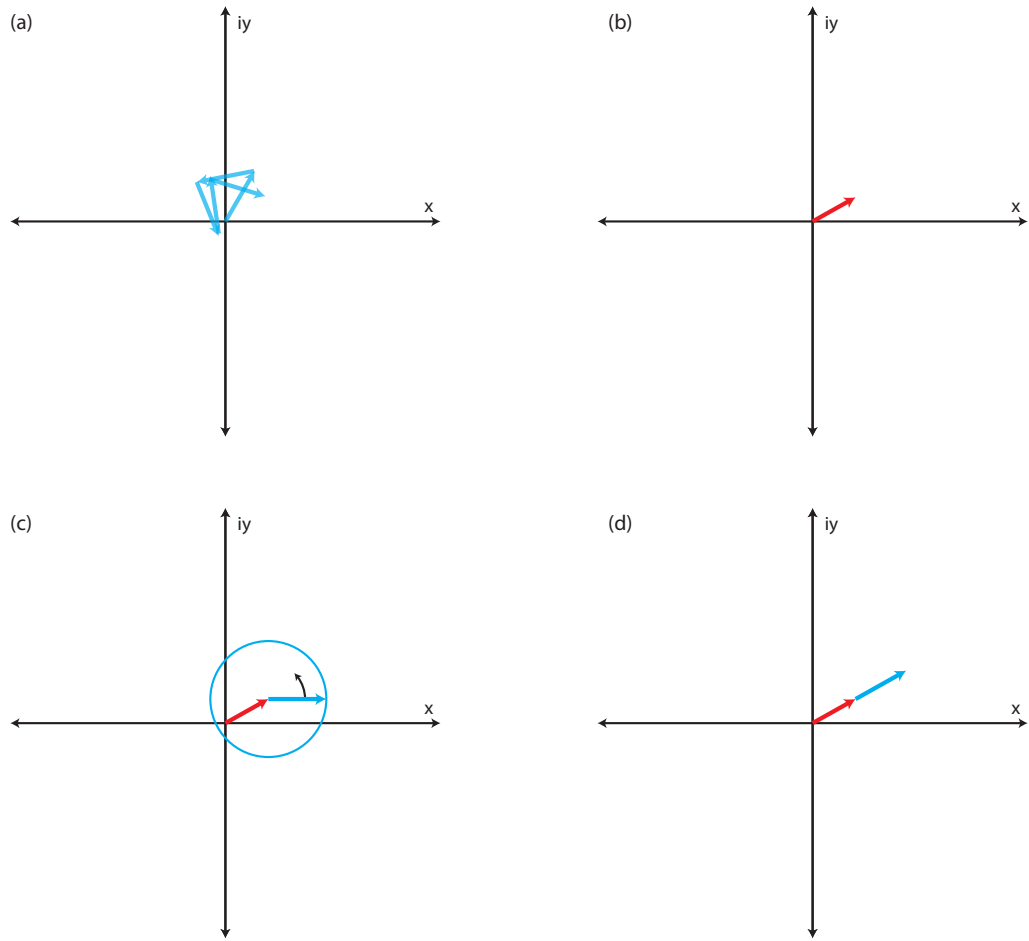


Figure 5.5: Phased array alignment routine. **a.** Random as-fabricated channel outputs as vectors in the complex plane. **b.** Sum of vectors in (a). **c.** Rotation of channel m about the summed vector of the other $N-1$ channels. **d.** Aligned phases after setting channel to maximize power at the detector.

We find the set of ϕ_n through a sequential optimization procedure. Note that for a chosen channel m ,

$$E_{det} = a_m e^{i\phi_m} + \sum_{n \neq m} a_n e^{i\phi_n} \quad (5.2)$$

By default, because of fabrication variations, ϕ_n are essentially random, and these vectors sum to a small value pointing at some random angle $\bar{\phi}$ (Figure 5.5 a,b).

We can, without loss of generality, set that angle $\bar{\phi}$ to zero, such that:

$$E_{det} = a_m e^{i\phi_m} + A \quad (5.3)$$

for real A . Assuming fully-independent phase control channels, we can drive channel m through several π , rotating that vector about the tip of the summed vectors A (Figure 5.5c), and measuring the received power at the detector:

$$I_{det} = |E_{det}|^2 = |A + e^{i\phi_m}|^2 = A^2 + a_m^2 + 2Aa_m \cos \phi_m \quad (5.4)$$

This is a sinusoidal modulation on top of a large DC background, where the optimum (aligned) ϕ_m occurs at the maximum of the curve. We can then go through each channel sequentially, setting it to the maximum, and will at the end of the procedure have all vectors aligned in-phase, maximizing power at the detector.

This system is essentially a large unbalanced 1:(N-1) Mach-Zehnder interferometer (Figure 5.4b). Fitting the cosine curve gives other parameters, as well: a_m , the relative amplitude of the modulated emitter, and V_π or P_π , the phase shifter efficiency, from the period of the signal.

One issue with this method (and similarly, essentially all channel-wise search methods) is the large SNR required when N becomes large and the random channels swamp the contribution of the modulated channel, especially as the phases become close to aligned and $A \gg a_m$. The required SNR is roughly equal to one over the interference visibility:

$$\text{Visibility} = \frac{2Aa_m}{a_m^2 + A^2} \approx \frac{2a_m}{A} \quad (5.5)$$

This SNR requirement is offset somewhat by the ability to do least-squares curve fitting on the measured cosine values. A large number of measurements at different phases can reduce the uncertainty in the proper phase setting even if amplitude noise is high; gradient search or other brute-force optimization methods (particularly those that rely on numerical derivatives) have no such smoothing and tend to be extremely sensitive to noisy measurements. Typical power versus swept phase curves are shown in Figure 5.6 for a 64-channel array.

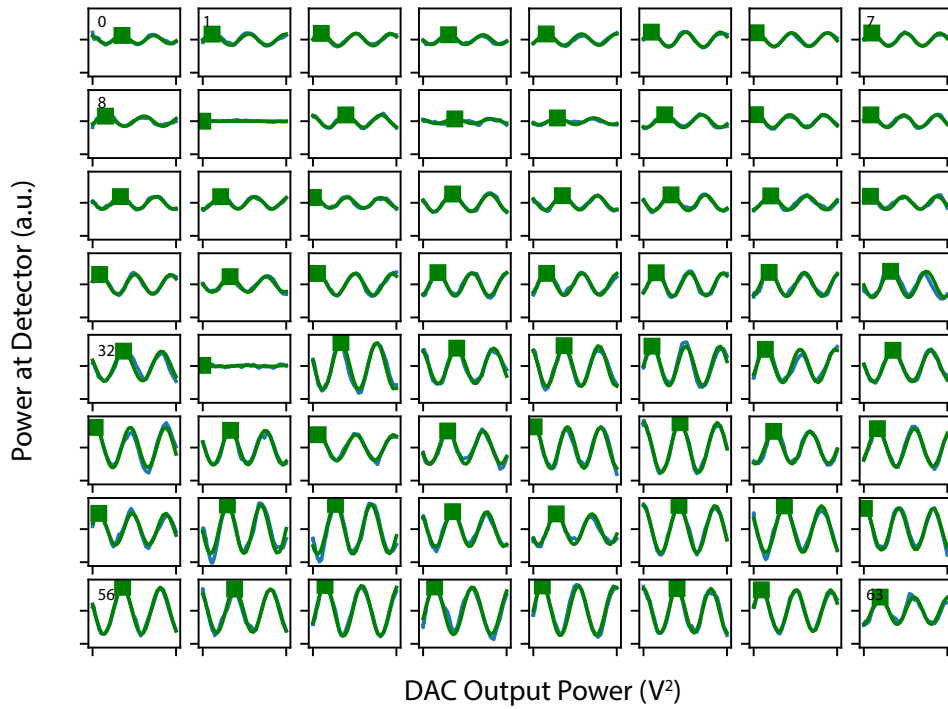


Figure 5.6: Swept voltage curves for phase calibration. Voltage for each channel is swept from 0 to 10 V, one channel after the next, and the resulting change in power is fit to $a \sin^2 P_\pi V^2$. Experimental data is blue, \sin^2 fit is green. Green square is the optimum voltage (lowest-voltage peak) that is set to form the final beam. Amplitude in later channels is larger as the beam becomes more converged and phases are better-aligned. Channels 9 and 33 have electrically-open phase shifters and so show no phase change with swept voltage.

BIBLIOGRAPHY

- [1] Andrew Rickman. The commercialization of silicon photonics. *Nature Photonics*, 8(8):579–582, August 2014.
- [2] David Thomson, Aaron Zilkie, John E. Bowers, Tin Komljenovic, Graham T. Reed, Laurent Vivien, Delphine Marris-Morini, Eric Cassan, Lopold Virost, Jean-Marc Fdli, Jean-Michel Hartmann, Jens H. Schmid, Dan-Xia Xu, Frdric Boeuf, Peter OBrien, Goran Z. Mashanovich, and M. Nedeljkovic. Roadmap on silicon photonics. *Journal of Optics*, 18(7):073003, 2016.
- [3] A. E. J. Lim, J. Song, Q. Fang, C. Li, X. Tu, N. Duan, K. K. Chen, R. P. C. Tern, and T. Y. Liow. Review of Silicon Photonics Foundry Efforts. *IEEE Journal of Selected Topics in Quantum Electronics*, 20(4):405–416, July 2014.
- [4] Peter Christy. Intel’s Silicon Photonics Products Could Change the World of IT, June 2016.
- [5] Qianfan Xu, Bradley Schmidt, Sameer Pradhan, and Michal Lipson. Micrometre-scale silicon electro-optic modulator. *Nature*, 435(7040):325–327, May 2005.
- [6] S. J. Spector, C. M. Sorace, M. W. Geis, M. E. Grein, J. U. Yoon, T. M. Lyszczarz, E. P. Ippen, and F. X. Krtner. Operation and Optimization of Silicon-Diode-Based Optical Modulators. *IEEE Journal of Selected Topics in Quantum Electronics*, 16(1):165–172, January 2010.
- [7] Alexander Gondarenko, Jacob S. Levy, and Michal Lipson. High confinement micron-scale silicon nitride high Q ring resonator. *Optics Express*, 17(14):11366–11370, July 2009.
- [8] Yoshitomo Okawachi, Kasturi Saha, Jacob S. Levy, Y. Henry Wen, Michal Lipson, and Alexander L. Gaeta. Octave-spanning frequency comb generation in a silicon nitride chip. *Optics Letters*, 36(17):3398–3400, September 2011.
- [9] Nicolas Sherwood-Droz and Michal Lipson. Scalable 3d dense integration of photonics on bulk silicon. *Optics Express*, 19(18):17758, August 2011.
- [10] Aseema Mohanty, Mian Zhang, Avik Dutt, Sven Ramelow, Paulo Nussenzeig, and Michal Lipson. Quantum interference between transverse spatial waveguide modes. *Nature Communications*, 8, January 2017.

- [11] K. I. Bolotin, K. J. Sikes, Z. Jiang, M. Klima, G. Fudenberg, J. Hone, P. Kim, and H. L. Stormer. Ultrahigh electron mobility in suspended graphene. *Solid State Communications*, 146(9):351–355, June 2008.
- [12] Alexander S. Mayorov, Roman V. Gorbachev, Sergey V. Morozov, Liam Britnell, Rashid Jalil, Leonid A. Ponomarenko, Peter Blake, Kostya S. Novoselov, Kenji Watanabe, Takashi Taniguchi, and A. K. Geim. Micrometer-Scale Ballistic Transport in Encapsulated Graphene at Room Temperature. *Nano Letters*, 11(6):2396–2399, June 2011.
- [13] Alexander Urich, Karl Unterrainer, and Thomas Mueller. Intrinsic Response Time of Graphene Photodetectors. *Nano Letters*, 11(7):2804–2808, July 2011.
- [14] Andreas Pospischil, Markus Humer, Marco M. Furchi, Dominic Bachmann, Romain Guider, Thomas Fromherz, and Thomas Mueller. CMOS-compatible graphene photodetector covering all optical communication bands. *Nature Photonics*, 7(11):892–896, September 2013.
- [15] Xuetao Gan, Ren-Jye Shiue, Yuanda Gao, Inanc Meric, Tony F. Heinz, Kenneth Shepard, James Hone, Solomon Assefa, and Dirk Englund. Chip-integrated ultrafast graphene photodetector with high responsivity. *Nature Photonics*, 7(11):883–887, November 2013.
- [16] Daniel Schall, Daniel Neumaier, Muhammad Mohsin, Bartos Chmielak, Jens Bolten, Caroline Porschatis, Andreas Prinzen, Christopher Mathiesen, Wolfgang Kuebart, Bernhard Junginger, Wolfgang Templ, Anna Lena Giesecke, and Heinrich Kurz. 50 GBit/s Photodetectors Based on Wafer-Scale Graphene for Integrated Silicon Photonic Communication Systems. *ACS Photonics*, 1(9):781–784, September 2014.
- [17] F. H. L. Koppens, T. Mueller, Ph Avouris, A. C. Ferrari, M. S. Vitiello, and M. Polini. Photodetectors based on graphene, other two-dimensional materials and hybrid systems. *Nature Nanotechnology*, 9(10):780–793, October 2014.
- [18] Ren-Jye Shiue, Yuanda Gao, Yifei Wang, Cheng Peng, Alexander D. Robertson, Dmitri K. Efetov, Solomon Assefa, Frank H. L. Koppens, James Hone, and Dirk Englund. High-Responsivity GrapheneBoron Nitride Photodetector and Autocorrelator in a Silicon Photonic Integrated Circuit. *Nano Letters*, 15(11):7288–7293, November 2015.

- [19] C. H. Cox, E. I. Ackerman, G. E. Betts, and J. L. Prince. Limits on the performance of RF-over-fiber links and their impact on device design. *IEEE Transactions on Microwave Theory and Techniques*, 54(2):906–920, February 2006.
- [20] H. H. Li. Refractive index of silicon and germanium and its wavelength and temperature derivatives. *Journal of Physical and Chemical Reference Data*, 9(3):561–658, July 1980.
- [21] I. H. Malitson. Interspecimen Comparison of the Refractive Index of Fused Silica. *JOSA*, 55(10):1205–1209, October 1965.
- [22] Marc J Madou. *Fundamentals of microfabrication and nanotechnology*. CRC Press, Boca Raton, FL, 3rd ed. edition, 2012.
- [23] John D. Joannopoulos, Steven G. Johnson, Joshua N. Winn, and Robert D. Meade. *Photonic Crystals: Molding the Flow of Light*. Princeton University Press, Princeton, NJ, 2008.
- [24] Allan W. Snyder and John D. Love. *Optical Waveguide Theory*. Springer US, Boston, MA, 1984. DOI: 10.1007/978-1-4613-2813-1.
- [25] Amnon Yariv and Pochi Yeh. *Photonics: Optical Electronics in Modern Communications*. Oxford University Press, New York, NY, 6th edition, 2007.
- [26] Dominic F. Gallagher and Thomas P. Felici. Eigenmode expansion methods for simulation of optical propagation in photonics: pros and cons. In *Proceedings of SPIE*, volume 4987, pages 69–82, 2003.
- [27] Chris Mack. *Fundamental Principles of Optical Lithography: The Science of Microfabrication*. John Wiley & Sons, 1st edition, March 2008.
- [28] Alfred Kwok-Kit Wong. *Resolution enhancement techniques in optical lithography*. SPIE Press, Bellingham, Wash., 2001.
- [29] Xingchen Ji, Felipe A. S. Barbosa, Samantha P. Roberts, Avik Dutt, Jaime Cardenas, Yoshitomo Okawachi, Alex Bryant, Alexander L. Gaeta, and Michal Lipson. Ultra-low-loss on-chip resonators with sub-milliwatt parametric oscillation threshold. *Optica*, 4(6):619–624, June 2017.

- [30] Jaime Cardenas, Carl B. Poitras, Jacob T. Robinson, Kyle Preston, Long Chen, and Michal Lipson. Low loss etchless silicon photonic waveguides. *Optics Express*, 17(6):4752–4757, March 2009.
- [31] Lian-Wee Luo, Gustavo S. Wiederhecker, Jaime Cardenas, Carl Poitras, and Michal Lipson. High quality factor etchless silicon photonic ring resonators. *Optics Express*, 19(7):6284, March 2011.
- [32] Austin Griffith, Jaime Cardenas, Carl B. Poitras, and Michal Lipson. High quality factor and high confinement silicon resonators using etchless process. *Optics Express*, 20(19):21341–21345, September 2012.
- [33] Vilson R. Almeida, Roberto R. Panepucci, and Michal Lipson. Nanotaper for compact mode conversion. *Optics Letters*, 28(15):1302–1304, August 2003.
- [34] J. Cardenas, C. B. Poitras, K. Luke, L. W. Luo, P. A. Morton, and M. Lipson. High Coupling Efficiency Etched Facet Tapers in Silicon Waveguides. *IEEE Photonics Technology Letters*, 26(23):2380–2382, December 2014.
- [35] Hermann A. Haus. *Waves and fields in optoelectronics*. Prentice-Hall, Englewood Cliffs, NJ, 1984.
- [36] H. Haus, W. Huang, S. Kawakami, and N. Whitaker. Coupled-mode theory of optical waveguides. *Journal of Lightwave Technology*, 5(1):16–23, January 1987.
- [37] Kane Yee. Numerical solution of initial boundary value problems involving maxwell’s equations in isotropic media. *IEEE Transactions on Antennas and Propagation*, 14(3):302–307, May 1966.
- [38] Ardavan F. Oskooi, David Roundy, Mihai Ibanescu, Peter Bermel, J. D. Joannopoulos, and Steven G. Johnson. Meep: A flexible free-software package for electromagnetic simulations by the FDTD method. *Computer Physics Communications*, 181(3):687–702, March 2010.
- [39] A. Yariv. Critical coupling and its control in optical waveguide-ring resonator systems. *IEEE Photonics Technology Letters*, 14(4):483–485, April 2002.
- [40] A. Yariv. Universal relations for coupling of optical power between microresonators and dielectric waveguides. *Electronics Letters*, 36(4):321–322, February 2000.

- [41] M. Iqbal, M. A. Gleeson, B. Spaugh, F. Tybor, W. G. Gunn, M. Hochberg, T. Baehr-Jones, R. C. Bailey, and L. C. Gunn. Label-Free Biosensor Arrays Based on Silicon Ring Resonators and High-Speed Optical Scanning Instrumentation. *IEEE Journal of Selected Topics in Quantum Electronics*, 16(3):654–661, May 2010.
- [42] Arthur Nitkowski, Antje Baeumner, and Michal Lipson. On-chip spectrophotometry for bioanalysis using microring resonators. *Biomedical Optics Express*, 2(2):271–277, February 2011.
- [43] Bernardo B. C. Kyotoku, Long Chen, and Michal Lipson. Sub-nm resolution cavity enhanced micro-spectrometer. *Optics Express*, 18(1):102–107, January 2010.
- [44] Ashim Dhakal, Ananth Z. Subramanian, Pieter Wuytens, Frdric Peyskens, Nicolas Le Thomas, and Roel Baets. Evanescent excitation and collection of spontaneous Raman spectra using silicon nitride nanophotonic waveguides. *Optics Letters*, 39(13):4025–4028, July 2014.
- [45] Qianfan Xu, Sasikanth Manipatruni, Brad Schmidt, Jagat Shakya, and Michal Lipson. 12.5 Gbit/s carrier-injection-based silicon micro-ring silicon modulators. *Optics Express*, 15(2):430, January 2007.
- [46] B. E. Little, J. S. Foresi, G. Steinmeyer, E. R. Thoen, S. T. Chu, H. A. Haus, E. P. Ippen, L. C. Kimerling, and W. Greene. Ultra-compact Si-SiO₂ microring resonator optical channel dropping filters. *IEEE Photonics Technology Letters*, 10(4):549–551, April 1998.
- [47] M. A. Popovic, T. Barwicz, M. S. Dahlem, F. Gan, C. W. Holzwarth, P. T. Rakich, M. R. Watts, H. I. Smith, F. X. Kartner, and E. P. Ippen. Hitless-Reconfigurable and Bandwidth-Scalable Silicon Photonic Circuits for Telecom and Interconnect Applications. In *OFC/NFOEC 2008 - 2008 Conference on Optical Fiber Communication/National Fiber Optic Engineers Conference*, pages 1–3, February 2008.
- [48] B. G. Lee, A. Biberman, J. Chan, and K. Bergman. High-Performance Modulators and Switches for Silicon Photonic Networks-on-Chip. *IEEE Journal of Selected Topics in Quantum Electronics*, 16(1):6–22, January 2010.
- [49] Yurii Vlasov, William M. J. Green, and Fengnian Xia. High-throughput silicon nanophotonic wavelength-insensitive switch for on-chip optical networks. *Nature Photonics*, 2(4):nphoton.2008.31, March 2008.

- [50] Brian Stern, Xiaoliang Zhu, Christine P. Chen, Lawrence D. Tzuang, Jaime Cardenas, Keren Bergman, and Michal Lipson. On-chip mode-division multiplexing switch. *Optica*, 2(6):530–535, June 2015.
- [51] Di Liang, Marco Fiorentino, Tadashi Okumura, Hsu-Hao Chang, Daryl T. Spencer, Ying-Hao Kuo, Alexander W. Fang, Daoxin Dai, Raymond G. Beausoleil, and John E. Bowers. Electrically-pumped compact hybrid silicon microring lasers for optical interconnects. *Optics Express*, 17(22):20355–20364, October 2009.
- [52] J. C. Hulme, J. K. Doyle, and J. E. Bowers. Widely tunable Vernier ring laser on hybrid silicon. *Optics Express*, 21(17):19718–19722, August 2013.
- [53] Brian Stern, Xingchen Ji, Avik Dutt, and Michal Lipson. Compact narrow-linewidth integrated laser based on a low-loss silicon nitride ring resonator. *Optics Letters*, 42(21):4541, November 2017.
- [54] Zhiping Zhou, Bing Yin, and Jurgen Michel. On-chip light sources for silicon photonics. *Light: Science & Applications*, 4(11):e358, November 2015.
- [55] Mark A. Foster, Amy C. Turner, Jay E. Sharping, Bradley S. Schmidt, Michal Lipson, and Alexander L. Gaeta. Broad-band optical parametric gain on a silicon photonic chip. *Nature*, 441(7096):nature04932, June 2006.
- [56] Jacob S. Levy, Alexander Gondarenko, Mark A. Foster, Amy C. Turner-Foster, Alexander L. Gaeta, and Michal Lipson. CMOS-compatible multiple-wavelength oscillator for on-chip optical interconnects. *Nature Photonics*, 4(1):nphoton.2009.259, December 2009.
- [57] Li Fan, Jian Wang, Leo T. Varghese, Hao Shen, Ben Niu, Yi Xuan, Andrew M. Weiner, and Minghao Qi. An All-Silicon Passive Optical Diode. *Science*, 335(6067):447–450, January 2012.
- [58] W. Bogaerts, P. De Heyn, T. Van Vaerenbergh, K. De Vos, S. Kumar Selvaraja, T. Claes, P. Dumon, P. Bienstman, D. Van Thourhout, and R. Baets. Silicon microring resonators. *Laser & Photonics Reviews*, 6(1):47–73, January 2012.
- [59] P. Rabiei, W. H. Steier, Cheng Zhang, and L. R. Dalton. Polymer micro-ring filters and modulators. *Journal of Lightwave Technology*, 20(11):1968–1975, November 2002.

- [60] Nicholas George. *Fourier Optics*. University of Rochester, Rochester, NY, December 2012.
- [61] C. J. Bouwkamp. Diffraction Theory. *Reports on Progress in Physics*, 17(1):35, 1954.
- [62] W. R. Smythe. The Double Current Sheet in Diffraction. *Physical Review*, 72(11):1066–1070, December 1947.
- [63] Lukas Novotny and Bert Hecht. *Principles of Nano-Optics*. Cambridge University Press, Cambridge, 2nd edition, 2012.
- [64] Constantine A. Balanis. *Antenna Theory - Analysis and Design*. John Wiley & Sons, Hoboken, NJ, 4th edition, 2016.
- [65] K. S. Novoselov, V. I. Falko, L. Colombo, P. R. Gellert, M. G. Schwab, and K. Kim. A roadmap for graphene. *Nature*, 490(7419):192–200, October 2012.
- [66] F. Bonaccorso, Z. Sun, T. Hasan, and A. C. Ferrari. Graphene photonics and optoelectronics. *Nature Photonics*, 4(9):nphoton.2010.186, August 2010.
- [67] Kin Fai Mak, Matthew Y. Sfeir, Yang Wu, Chun Hung Lui, James A. Misewich, and Tony F. Heinz. Measurement of the Optical Conductivity of Graphene. *Physical Review Letters*, 101(19):196405, November 2008.
- [68] Steven J. Koester and Mo Li. High-speed waveguide-coupled graphene-on-graphene optical modulators. *Applied Physics Letters*, 100(17):171107, April 2012.
- [69] Jacek Gosciniaik and Dawn T. H. Tan. Theoretical investigation of graphene-based photonic modulators. *Scientific Reports*, 3:srep01897, May 2013.
- [70] Ming Liu, Xiaobo Yin, Erick Ulin-Avila, Baisong Geng, Thomas Zentgraf, Long Ju, Feng Wang, and Xiang Zhang. A graphene-based broadband optical modulator. *Nature*, 474(7349):64–67, June 2011.
- [71] Ming Liu, Xiaobo Yin, and Xiang Zhang. Double-Layer Graphene Optical Modulator. *Nano Letters*, 12(3):1482–1485, March 2012.
- [72] Nathan Youngblood, Yoska Anugrah, Rui Ma, Steven J. Koester, and Mo Li. Multifunctional Graphene Optical Modulator and Photodetector Integrated on Silicon Waveguides. *Nano Letters*, 14(5):2741–2746, May 2014.

- [73] Muhammad Mohsin, Daniel Schall, Martin Otto, Achim Nocolak, Daniel Neumaier, and Heinrich Kurz. Graphene based low insertion loss electro-absorption modulator on SOI waveguide. *Optics Express*, 22(12):15292–15297, June 2014.
- [74] Ciyuan Qiu, Weilu Gao, Robert Vajtai, Pulickel M. Ajayan, Junichiro Kono, and Qianfan Xu. Efficient Modulation of 1.55 μm Radiation with Gated Graphene on a Silicon Microring Resonator. *Nano Letters*, 14(12):6811–6815, December 2014.
- [75] Y. T. Hu, M. Pantouvaki, S. Brems, I. Asselberghs, C. Huyghebaert, M. Geisler, C. Alessandri, R. Baets, P. Absil, D. Van Thourhout, and J. Van Campenhout. Broadband 10gb/s graphene electro-absorption modulator on silicon for chip-level optical interconnects. In *2014 IEEE International Electron Devices Meeting*, pages 5.6.1–5.6.4, December 2014.
- [76] B. C. Jacobs and J. D. Franson. All-optical switching using the quantum Zeno effect and two-photon absorption. *Physical Review A*, 79(6):063830, June 2009.
- [77] Feng Wang, Yuanbo Zhang, Chuanshan Tian, Caglar Girit, Alex Zettl, Michael Crommie, and Y. Ron Shen. Gate-Variable Optical Transitions in Graphene. *Science*, 320(5873):206–209, April 2008.
- [78] Y. Henry Wen, Onur Kuzucu, Taige Hou, Michal Lipson, and Alexander L. Gaeta. All-optical switching of a single resonance in silicon ring resonators. *Optics Letters*, 36(8):1413–1415, April 2011.
- [79] Michele Midrio, Stefano Boscolo, Michele Moresco, Marco Romagnoli, Costantino De Angelis, Andrea Locatelli, and Antonio-Daniele Capobianco. Grapheneassisted criticallycoupled optical ring modulator. *Optics Express*, 20(21):23144–23155, October 2012.
- [80] N. Gruhler, C. Benz, H. Jang, J.-H. Ahn, R. Danneau, and W. H. P. Pernice. High-quality Si_3N_4 circuits as a platform for graphene-based nanophotonic devices. *Optics Express*, 21(25):31678–31689, December 2013.
- [81] Li Fan, Leo T. Varghese, Yi Xuan, Jian Wang, Ben Niu, and Minghao Qi. Direct fabrication of silicon photonic devices on a flexible platform and its application for strain sensing. *Optics Express*, 20(18):20564–20575, August 2012.

- [82] Xuesong Li, Weiwei Cai, Jinho An, Seyoung Kim, Junghyo Nah, Dongxing Yang, Richard Piner, Aruna Velamakanni, Inhwa Jung, Emanuel Tutuc, Sanjay K. Banerjee, Luigi Colombo, and Rodney S. Ruoff. Large-Area Synthesis of High-Quality and Uniform Graphene Films on Copper Foils. *Science*, 324(5932):1312–1314, June 2009.
- [83] Xuelei Liang, Brent A. Sperling, Irene Calizo, Guangjun Cheng, Christina Ann Hacker, Qin Zhang, Yaw Obeng, Kai Yan, Hailin Peng, Qiliang Li, Xiaoxiao Zhu, Hui Yuan, Angela R. Hight Walker, Zhongfan Liu, Lian-mao Peng, and Curt A. Richter. Toward Clean and Crackless Transfer of Graphene. *ACS Nano*, 5(11):9144–9153, November 2011.
- [84] A. Das, S. Pisana, B. Chakraborty, S. Piscanec, S. K. Saha, U. V. Waghmare, K. S. Novoselov, H. R. Krishnamurthy, A. K. Geim, A. C. Ferrari, and A. K. Sood. Monitoring dopants by Raman scattering in an electrochemically top-gated graphene transistor. *Nature Nanotechnology*, 3(4):210–215, April 2008.
- [85] Wei Li, Yiran Liang, Dangmin Yu, Lianmao Peng, Kurt P. Pernstich, Tian Shen, A. R. Hight Walker, Guangjun Cheng, Christina A. Hacker, Curt A. Richter, Qiliang Li, David J. Gundlach, and Xuelei Liang. Ultraviolet/ozone treatment to reduce metal-graphene contact resistance. *Applied Physics Letters*, 102(18):183110, May 2013.
- [86] Wei Li, Christina A. Hacker, Guangjun Cheng, Yiran Liang, Boyuan Tian, A. R. Hight Walker, Curt A. Richter, David J. Gundlach, Xuelei Liang, and Lianmao Peng. Highly reproducible and reliable metal/graphene contact by ultraviolet-ozone treatment. *Journal of Applied Physics*, 115(11):114304, March 2014.
- [87] Joshua A. Robinson, Michael LaBella, Mike Zhu, Matt Hollander, Richard Kasarda, Zachary Hughes, Kathleen Trumbull, Randal Cavalero, and David Snyder. Contacting graphene. *Applied Physics Letters*, 98(5):053103, January 2011.
- [88] Yung-Chang Lin, Chun-Chieh Lu, Chao-Huei Yeh, Chuanhong Jin, Kazu Suenaga, and Po-Wen Chiu. Graphene Annealing: How Clean Can It Be? *Nano Letters*, 12(1):414–419, January 2012.
- [89] A. Hsu, H. Wang, K. K. Kim, J. Kong, and T. Palacios. Impact of Graphene Interface Quality on Contact Resistance and RF Device Performance. *IEEE Electron Device Letters*, 32(8):1008–1010, August 2011.

- [90] Joshua D. Wood, Gregory P. Doidge, Enrique A. Carrion, Justin C. Koepke, Joshua A. Kaitz, Isha Datye, Ashkan Behnam, Jayan Hewaparakrama, Basil Aruin, Yaofeng Chen, Hefei Dong, Richard T. Haasch, Joseph W. Lyding, and Eric Pop. Annealing free, clean graphene transfer using alternative polymer scaffolds. *Nanotechnology*, 26(5):055302, 2015.
- [91] Wei-Hsiang Lin, Ting-Hui Chen, Jan-Kai Chang, Jieh-I Taur, Yuan-Yen Lo, Wei-Li Lee, Chia-Seng Chang, Wei-Bin Su, and Chih-I Wu. A Direct and Polymer-Free Method for Transferring Graphene Grown by Chemical Vapor Deposition to Any Substrate. *ACS Nano*, 8(2):1784–1791, February 2014.
- [92] Bin Wang, Ming Huang, Li Tao, Sun Hwa Lee, A-Rang Jang, Bao-Wen Li, Hyeon Suk Shin, Deji Akinwande, and Rodney S. Ruoff. Support-Free Transfer of Ultrasoother Graphene Films Facilitated by Self-Assembled Monolayers for Electronic Devices and Patterns. *ACS Nano*, 10(1):1404–1410, January 2016.
- [93] Guohui Zhang, Aleix G. Gell, Paul M. Kirkman, Robert A. Lazenby, Thomas S. Miller, and Patrick R. Unwin. Versatile Polymer-Free Graphene Transfer Method and Applications. *ACS Applied Materials & Interfaces*, 8(12):8008–8016, March 2016.
- [94] L. Wang, I. Meric, P. Y. Huang, Q. Gao, Y. Gao, H. Tran, T. Taniguchi, K. Watanabe, L. M. Campos, D. A. Muller, J. Guo, P. Kim, J. Hone, K. L. Shepard, and C. R. Dean. One-Dimensional Electrical Contact to a Two-Dimensional Material. *Science*, 342(6158):614–617, November 2013.
- [95] Wei Sun Leong, Hao Gong, and John T. L. Thong. Low-Contact-Resistance Graphene Devices with Nickel-Etched-Graphene Contacts. *ACS Nano*, 8(1):994–1001, January 2014.
- [96] Joshua T. Smith, Aaron D. Franklin, Damon B. Farmer, and Christos D. Dimitrakopoulos. Reducing Contact Resistance in Graphene Devices through Contact Area Patterning. *ACS Nano*, 7(4):3661–3667, April 2013.
- [97] Arka Majumdar, Jonghwan Kim, Jelena Vuckovic, and Feng Wang. Electrical Control of Silicon Photonic Crystal Cavity by Graphene. *Nano Letters*, 13(2):515–518, February 2013.
- [98] Xuetao Gan, Ren-Jye Shiue, Yuanda Gao, Kin Fai Mak, Xinwen Yao, Luozhou Li, Attila Szep, Dennis Walker, James Hone, Tony F. Heinz, and Dirk Englund. High-Contrast Electrooptic Modulation of a Photonic Crystal

Nanocavity by Electrical Gating of Graphene. *Nano Letters*, 13(2):691–696, February 2013.

- [99] Yuanda Gao, Ren-Jye Shiue, Xuetao Gan, Luozhou Li, Cheng Peng, Inanc Meric, Lei Wang, Attila Szep, Dennis Walker, James Hone, and Dirk Englund. High-Speed Electro-Optic Modulator Integrated with Graphene-Boron Nitride Heterostructure and Photonic Crystal Nanocavity. *Nano Letters*, 15(3):2001–2005, March 2015.
- [100] Matthew Streshinsky, Ali Ayazi, Zhe Xuan, Andy Eu-Jin Lim, Guo-Qiang Lo, Tom Baehr-Jones, and Michael Hochberg. Highly linear silicon traveling wave Mach-Zehnder carrier depletion modulator based on differential drive. *Optics Express*, 21(3):3818–3825, February 2013.
- [101] Jaime Cardenas, Paul A. Morton, Jacob B. Khurgin, Austin Griffith, Carl B. Poitras, Kyle Preston, and Michal Lipson. Linearized silicon modulator based on a ring assisted Mach Zehnder inteferometer. *Optics Express*, 21(19):22549–22557, September 2013.
- [102] A. M. Gutierrez, J. V. Galan, J. Herrera, A. Brimont, D. Marris-Morini, J. M. Fdli, L. Vivien, and P. Sanchis. High linear ring-assisted MZI electro-optic silicon modulators suitable for radio-over-fiber applications. In *The 9th International Conference on Group IV Photonics (GFP)*, pages 57–59, August 2012.
- [103] Y. H. Daniel Lee, J. Cardenas, and M. Lipson. Linear silicon PN junction phase modulator. In *2015 Conference on Lasers and Electro-Optics (CLEO)*, pages 1–2, May 2015.
- [104] Bin Liu, Jongin Shim, Yi-Jen Chiu, A. Keating, J. Piprek, and J. E. Bowers. Analog characterization of low-voltage MQW traveling-wave electroabsorption modulators. *Journal of Lightwave Technology*, 21(12):3011–3019, December 2003.
- [105] G. E. Betts, C. H. Cox, and K. G. Ray. 20 GHz optical analog link using an external modulator. *IEEE Photonics Technology Letters*, 2(12):923–925, December 1990.
- [106] Shaffique Adam, E. H. Hwang, V. M. Galitski, and S. Das Sarma. A self-consistent theory for graphene transport. *Proceedings of the National Academy of Sciences*, 104(47):18392–18397, November 2007.

- [107] K. I. Bolotin, K. J. Sikes, J. Hone, H. L. Stormer, and P. Kim. Temperature-Dependent Transport in Suspended Graphene. *Physical Review Letters*, 101(9), August 2008.
- [108] Z. Q. Li, E. A. Henriksen, Z. Jiang, Z. Hao, M. C. Martin, P. Kim, H. L. Stormer, and D. N. Basov. Dirac charge dynamics in graphene by infrared spectroscopy. *Nature Physics*, 4(7):532–535, July 2008.
- [109] J. Martin, N. Akerman, G. Ulbricht, T. Lohmann, J. H. Smet, K. von Klitzing, and A. Yacoby. Observation of electronhole puddles in graphene using a scanning single-electron transistor. *Nature Physics*, 4(2):144–148, February 2008.
- [110] L. A. Ponomarenko, R. Yang, T. M. Mohiuddin, M. I. Katsnelson, K. S. Novoselov, S. V. Morozov, A. A. Zhukov, F. Schedin, E. W. Hill, and A. K. Geim. Effect of a High- κ Environment on Charge Carrier Mobility in Graphene. *Physical Review Letters*, 102(20):206603, May 2009.
- [111] Kristen M. Burson, William G. Cullen, Shaffique Adam, Cory R. Dean, K. Watanabe, T. Taniguchi, Philip Kim, and Michael S. Fuhrer. Direct Imaging of Charged Impurity Density in Common Graphene Substrates. *Nano Letters*, 13(8):3576–3580, August 2013.
- [112] C. R. Dean, A. F. Young, I. Meric, C. Lee, L. Wang, S. Sorgenfrei, K. Watanabe, T. Taniguchi, P. Kim, K. L. Shepard, and J. Hone. Boron nitride substrates for high-quality graphene electronics. *Nature Nanotechnology*, 5(10):722–726, October 2010.
- [113] Choongyu Hwang, David A. Siegel, Sung-Kwan Mo, William Regan, Ariel Ismach, Yuegang Zhang, Alex Zettl, and Alessandra Lanzara. Fermi velocity engineering in graphene by substrate modification. *Scientific Reports*, 2:srep00590, August 2012.
- [114] Zhimin Shi, Ksenia Dolgaleva, and Robert W Boyd. Quantum noise properties of non-ideal optical amplifiers and attenuators. *Journal of Optics*, 13(12):125201, December 2011.
- [115] Muhammad Mohsin, Daniel Neumaier, Daniel Schall, Martin Otto, Christopher Matheisen, Anna Lena Giesecke, Abhay A. Sagade, and Heinrich Kurz. Experimental verification of electro-refractive phase modulation in graphene. *Scientific Reports*, 5:srep10967, June 2015.

- [116] V. Sorianoello, G. De Angelis, T. Cassese, M. Midrio, M. Romagnoli, M. Mohsin, M. Otto, D. Neumaier, I. Asselberghs, J. Van Campenhout, and C. Huyghebaert. Complex effective index in graphene-silicon waveguides. *Optics Express*, 24(26):29984–29993, December 2016.
- [117] V. Sorianoello, M. Midrio, G. Contestabile, I. Asselberg, J. Van Campenhout, C. Huyghebaerts, I. Goykhman, A. K. Ott, A. C. Ferrari, and M. Romagnoli. Graphene Phase Modulator. *arXiv:1704.01525 [cond-mat]*, March 2017. arXiv: 1704.01525.
- [118] W.D. Sacher and J.K.S. Poon. Characteristics of Microring Resonators With Waveguide-Resonator Coupling Modulation. *Journal of Lightwave Technology*, 27(17):3800–3811, September 2009.
- [119] W. D. Sacher, W. M. J. Green, S. Assefa, T. Barwicz, H. Pan, S. M. Shank, Y. A. Vlasov, and J. K. S. Poon. Coupling modulation of microrings at rates beyond the linewidth limit. *Optics Express*, 21(8):9722, April 2013.
- [120] Jie Sun, Erman Timurdogan, Ami Yaacobi, Ehsan Shah Hosseini, and Michael R. Watts. Large-scale nanophotonic phased array. *Nature*, 493(7431):195–199, January 2013.
- [121] Jie Sun, Ehsan shah Hosseini, Ami Yaacobi, David B. Cole, Gerald Leake, Douglas Coolbaugh, and Michael R. Watts. Two-dimensional apodized silicon photonic phased arrays. *Optics Letters*, 39(2):367, January 2014.
- [122] Ami Yaacobi, Jie Sun, Michele Moresco, Gerald Leake, Douglas Coolbaugh, and Michael R. Watts. Integrated phased array for wide-angle beam steering. *Optics Letters*, 39(15):4575, August 2014.
- [123] J. C. Hulme, J. K. Doylend, M. J. R. Heck, J. D. Peters, M. L. Davenport, J. T. Bovington, L. A. Coldren, and J. E. Bowers. Fully integrated hybrid silicon two dimensional beam scanner. *Optics Express*, 23(5):5861, March 2015.
- [124] J. K. Doylend, M. J. R. Heck, J. T. Bovington, J. D. Peters, L. A. Coldren, and J. E. Bowers. Two-dimensional free-space beam steering with an optical phased array on silicon-on-insulator. *Optics Express*, 19(22):21595–21604, October 2011.
- [125] David N. Hutchison, Jie Sun, Jonathan K. Doylend, Ranjeet Kumar, John Heck, Woosung Kim, Christopher T. Phare, Avi Feshali, and Haisheng Rong.

- High-resolution aliasing-free optical beam steering. *Optica*, 3(8):887, August 2016.
- [126] Hooman Abediasl and Hossein Hashemi. Monolithic optical phased-array transceiver in a standard SOI CMOS process. *Optics Express*, 23(5):6509, March 2015.
- [127] Firooz Aflatouni, Behrooz Abiri, Angad Rekhi, and Ali Hajimiri. Nanophotonic projection system. *Optics Express*, 23(16):21012, August 2015.
- [128] Christopher V. Poulton, Matthew J. Byrd, Manan Raval, Zhan Su, Nanxi Li, Erman Timurdogan, Douglas Coolbaugh, Diedrik Vermeulen, and Michael R. Watts. Large-scale silicon nitride nanophotonic phased arrays at infrared and visible wavelengths. *Optics Letters*, 42(1):21, January 2017.
- [129] S. Chung, H. Abediasl, and H. Hashemi. A 1024-element scalable optical phased array in 0.18 μm SOI CMOS. In *2017 IEEE International Solid-State Circuits Conference (ISSCC)*, pages 262–263, February 2017.
- [130] S. Chung, H. Abediasl, and H. Hashemi. A Monolithically Integrated Large-Scale Optical Phased Array in Silicon-on-Insulator CMOS. *IEEE Journal of Solid-State Circuits*, PP(99):1–22, 2017.
- [131] Michael R. Kossey, Charbel Rizk, and Amy C. Foster. End-Fire Silicon Optical Phased Array with Half-Wavelength Spacing. *arXiv preprint arXiv:1706.01452*, 2017.
- [132] David Kwong, Amir Hosseini, John Covey, Yang Zhang, Xiaochuan Xu, Harish Subbaraman, and Ray T. Chen. On-chip silicon optical phased array for two-dimensional beam steering. *Optics Letters*, 39(4):941, February 2014.
- [133] Keyvan Sayyah, Oleg Efimov, Pamela Patterson, James Schaffner, Carson White, Jean-Francois Seurin, Guoyang Xu, and Alexander Miglo. Two-dimensional pseudo-random optical phased array based on tandem optical injection locking of vertical cavity surface emitting lasers. *Optics Express*, 23(15):19405–19416, July 2015.
- [134] C. T. DeRose, R. D. Kekatpure, D. C. Trotter, A. Starbuck, J. R. Wendt, A. Yaacobi, M. R. Watts, U. Chettiar, N. Engheta, and P. S. Davids. Electronically controlled optical beam-steering by an active phased array of metallic nanoantennas. *Optics Express*, 21(4):5198–5208, February 2013.

- [135] A. Vosoogh and P. S. Kildal. Simple Formula for Aperture Efficiency Reduction Due to Grating Lobes in Planar Phased Arrays. *IEEE Transactions on Antennas and Propagation*, 64(6):2263–2269, June 2016.
- [136] Dmitri K. Gramotnev and Sergey I. Bozhevolnyi. Plasmonics beyond the diffraction limit. *Nature Photonics*, 4(2):83–91, February 2010.
- [137] R. F. Oulton, V. J. Sorger, D. A. Genov, D. F. P. Pile, and X. Zhang. A hybrid plasmonic waveguide for subwavelength confinement and long-range propagation. *Nature Photonics*, 2(8):496–500, August 2008.
- [138] Tin Komljenovic, Roger Helkey, Larry Coldren, and John E. Bowers. Sparse aperiodic arrays for optical beam forming and LIDAR. *Optics Express*, 25(3):2511–2528, February 2017.
- [139] Weiwei Song, Robert Gatdula, Siamak Abbaslou, Ming Lu, Aaron Stein, Warren Y.-C. Lai, J. Provine, R. Fabian W. Pease, Demetrios N. Christodoulides, and Wei Jiang. High-density waveguide superlattices with low crosstalk. *Nature Communications*, 6:7027, May 2015.